INVESTIGATION OF HYPERVELOCITY MICROPARTICLES IMPACT PHENOMENA

By J. C. Slattery & N. L. Roy

TRW®
SYSTEMS GROUP
ONE SPACE PARK • REDONDO BEACH, CALIFORNIA

11489-6012-RO-00

NASA CR-66872

INVESTIGATION OF HYPERVELOCITY MICROPARTICLES IMPACT PHENOMENA

By J. C. Slattery & N. L. Roy

Prepared under Contract No. NAS 1-8299 by
TRW SYSTEMS GROUP
Redondo Beach, California

for

NATIONAL AERONAUTICS AND SPACE ADMINISTRATION

INVESTIGATION OF HYPERVELOCITY MICROPARTICLES IMPACT PHENOMENA

ABSTRACT

This report presents some of the experimental results obtained during the past year with a micrometeoroid linear accelerator. The linear accelerator accelerates metallic, micro-size particles to velocities up to 25 km/sec. Five experiments are included: (1) Impact light flash; (2) Thin-film capacitors; (3) Microphone sensors; (4) Cratering; (5) Thin-film penetration. Results are presented on the response of capacitor microphones to hypervelocity impact at velocities much higher than were previously possible. Much of the work on thin-film penetration was possible because relatively thick foils could be used at the higher velocities attainable with the linac; uniformly thick foils are easier to make than uniformly thin ones.

INVESTIGATION OF HYPERVELOCITY MICROPARTICLES IMPACT PHENOMENA

I. INTRODUCTION

The electrical acceleration technique is attractive as a launch method because very high velocities can be obtained with well-defined particles. However, the particles are limited in size and composition, i.e., they must be on the order of one micron in diameter and must be metallic. The size limitation presents many problems to the experimenter because data must be analyzed on the microscopic level.

Size limitation can be relaxed somewhat by increasing the accelerating voltages. It has been shown previously[1] that the radius of the accelerated particle is directly proportional to the total accelerating voltage at a constant velocity; for example, a larger particle can be accelerated to the same velocity as a smaller one by an appropriate increase in accelerating voltage.

Under a previous NASA contract[2] with Langley Research Center, TRW designed and constructed a microparticle linear accelerator with the objective of attaining a total accelerating voltage of 10 MV. The operating accelerator has been limited to about 7 MV due to the unsolved voltage breakdown problems. However, the voltage achieved represents a significant gain when compared to the 1.5 MV attained from our original Van de Graaff which is now used as an injector for the linear accelerator.

This report presents some of the experimental results obtained during the past year with the linear accelerator. Five experiments are included: (1) Impact light flash; (2) Thin-film capacitors; (3) Microphone sensors; (4) Cratering; (5) Thin-film penetration. Results are presented on the response of capacitor microphones to hypervelocity impact at velocities much higher than were previously possible. Much of the work on thin-film

penetration was possible because relatively thick foils could be used at the higher velocities attainable with the linac; uniformly thick foils are easier to make than uniformly thin ones.

2. LINEAR ACCELERATOR

Langley Research Center's accelerator was used for these experimental studies because it offers a significant increase in impact momentum, at a given velocity, over that available from electrostatic accelerators previously used. This is true even when operated at the conservative 7 million volts used during these experiments.

Particles were introduced into the Van de Graaff (VDG) generator, which supplied the initial energy necessary for injection into the linear accelerator (linac) (see Figure 6). A velocity selection system was placed on the output end of the VDG generator which allowed a small input velocity range to be selected before injection of the particles into the linac. A particle with the prescribed velocity requirements was detected by the sensors at the input end of the linac; these sensors then activated the system so that accelerating voltages were applied to the linac structure in the correct time relationship for that particular particle. The frequency generating electronics provided a ready means for oscilloscope triggering and display of the particle as it passed through the particle-charge detector before impact on the target. A second sweep was also triggered, which displayed the signal from the target as the particle struck it.

In a charged particle accelerator, the particles are first charged by passing them close to a high voltage probe.[1] The particles acquire approximately the same surface electric field strength as the probe. Next, the particle is introduced into the electrostatic field of the Van de Graaff, and is accelerated in a manner such that energy is conserved. From these facts

of operation, the particle mass (and the momentum) can be shown to vary directly with the cube of the accelerating voltage. The high accelerating voltage provided by the linac yields a remarkable increase in particle impact momentum, at this voltage the particle momentum is two orders of magnitude greater than the momentum available from the 1.5 million volt accelerator previously used. The particle charge (measured from the particle-charge detector), the particle velocity (measured by the linac frequency-generating electronics), and the total accelerating voltage provided the required data for calculation of particle parameters for each accelerated particle.

This report is not intended to describe the accelerator (reference 2 provides a full description of the machine) and operating details are excluded. In general, the machine operates stably and predictably and the repetition rate is about one particle every 30 seconds.

3. INTENSITY-TIME CHARACTERISTICS OF IMPACT LIGHT FLASH

A flash of light is emitted when a hypervelocity particle strikes a solid target. The impact light flash occurs with or without residual gas in the vicinity of the target. However, the light emitted from an impact is not independent of pressure.

Due to the nature of the accelerator being used for these impact studies, we are able to maintain relatively good vacuum conditions with ease. The pressure in the target chamber for this experiment, and all other experiments described in this report, was 2×10^{-5} Torr or lower. This pressure range is sufficiently low so that any light contribution from the particle or impact debris interacting with the residual gas should be neglible. At much higher pressures one would expect light to be emitted not only from the impact site, but also from the interaction of the debris with the residual gas.[3,4]

We have measured the time-intensity behavior of the impact light flash for both thick and thin targets. Each target was studied with both fast and slow particles. The fast particles were in excess of 20 km/sec (average about 25 km/sec) and the slow particles were below 10 km/sec (average about 4.5 km/sec). The thick target was a tantalum sheet and the thin target was an 800 Å gold foil without backing. Impacts occur normal to the target surface. They are viewed by a photomultiplier tube at an angle of 45° to the target located at a distance of approximately 10 cm from the impact site. This experiment utilized one viewport of the arrangement shown in Figure 3.

The photomultiplier tube used to record the flashes was an RCA 6199 with a RC time constant at the last dynode of less than 10 nanoseconds. The pre-amplifier and oscilloscope had a combined risetime of less than 10 nanoseconds. Because the fastest pulse risetime observed was about 25 nanoseconds, we believe that it was accurately recorded. The results are described semi-quantitatively in the following.

With the thick tantalum target and fast particles a typical light pulse appeared somewhat as sketched in Figure 1a. The light pulse has been shown on a relatively slow sweep speed and since the initial shape of the pulse is of interest this has been shown in the inset on an expanded time scale. The pulse reached a peak in about 25 to 30 nanoseconds. During the next 50 to 100 nano-seconds the signal decayed to about one-half the peak amplitude. This decay was followed by what seemed to be an exponential decay with an e-folding time of 20 to 40 microseconds. Thus, the signal persisted for about 100 microseconds.

When slow particles struck the thick tantalum target the typical light pulse changed slightly. An example is shown in Figure 1b. The pulse risetime was noticeably longer, being about 50 nanoseconds, and there was no evidence of the prominent peak, as shown in Figure 1a. The exponential decay which followed had about the time constant as that in Figure 1a; that is, about 20 to 40 microseconds. Thus this signal persisted for about 100 microseconds.

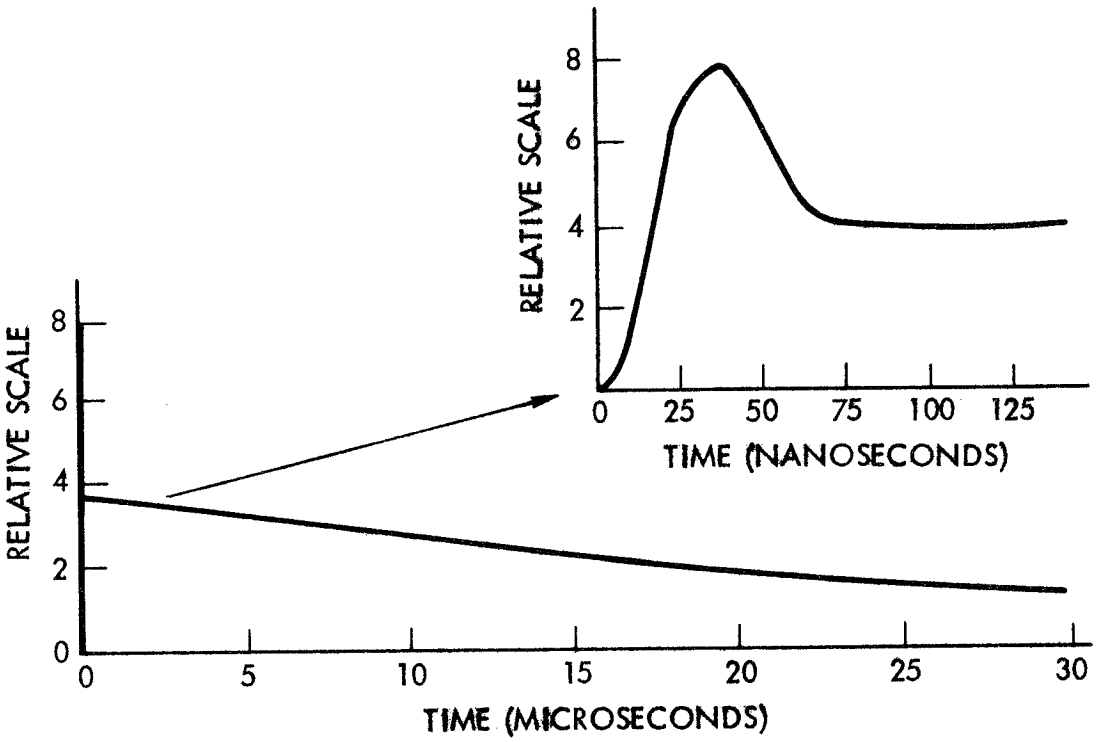

Figure 1a

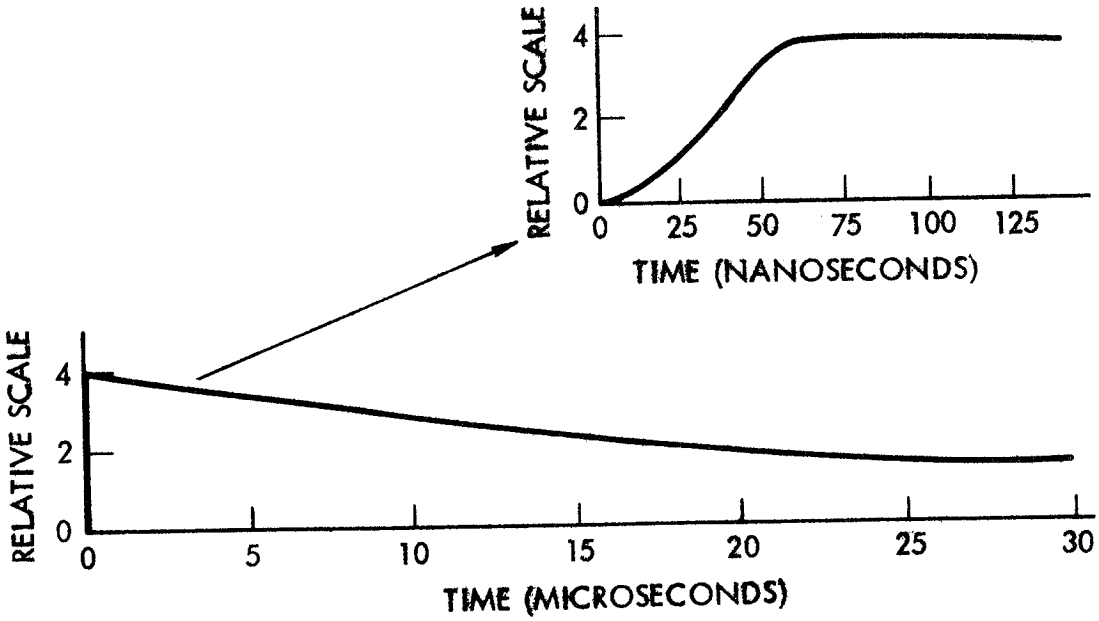

Figure 1b

Figure 1. Intensity-time behavior of impact light flash on a thick tantalum target with "fast" particles (Figure 1a) and "slow" particles (Figure 1b).

It would appear that the impact light flash observed above may be composed of light generated chiefly by two different mechanisms. It is known from previous work by this organization[3,5] that an "impact plasma" is generated at the time of a hypervelocity impact from which ionized particles may be extracted. This "plasma" is only weakly discernible at 5 km/sec by extracting the charge produced; however, the extracted charge is very strongly velocity dependent (V^3). This strong velocity dependence of the extracted charge implies that the plasma volume and/or plasma temperature is also strongly velocity dependent. We would like to suggest that the short duration light pulse produced with the high velocity particles is radiation emitted from the highly excited atoms in this plasma. The long duration light pulse is most likely the blackbody or continuum radiation associated with the hot crater and the ejected debris. This short duration pulse was not observed for the slow particles which seems to lend credence to this explanation. For the slow impacts then, the blackbody radiation is the chief source of light.

Figure 2a indicates the light pulse behavior with a thin target and fast particles. The signal has a large amplitude and is very clean. It has a rise-time of about 25 nanoseconds followed by what appears to be an exponential decay with an e-folding time of 60 to 70 nanoseconds. Some "hash" was evident for 1 to 2 microseconds, but the hash was gone in less than 5 microseconds, even when the gain was increased by a factor of ten.

Figure 2b is a sketch of the typical light pulse when slow particles strike the thin target. The pulse amplitude is down by a factor of about 20 from the fast particle pulse, even though the slow particles have at least 100 times more mass. The signal is not very clean, as indicated in Figure 2b, probably because of photon statistics. The risetime is about 50 nanoseconds and the signal decays essentially to zero in 1 to 1.5 microseconds. Some hash is evident, but it lasted no more than 10 to 20 microseconds.

The light pulse recorded for the thin target and fast particles is quite similar to the initial fast pulse recorded for fast particles into a thick

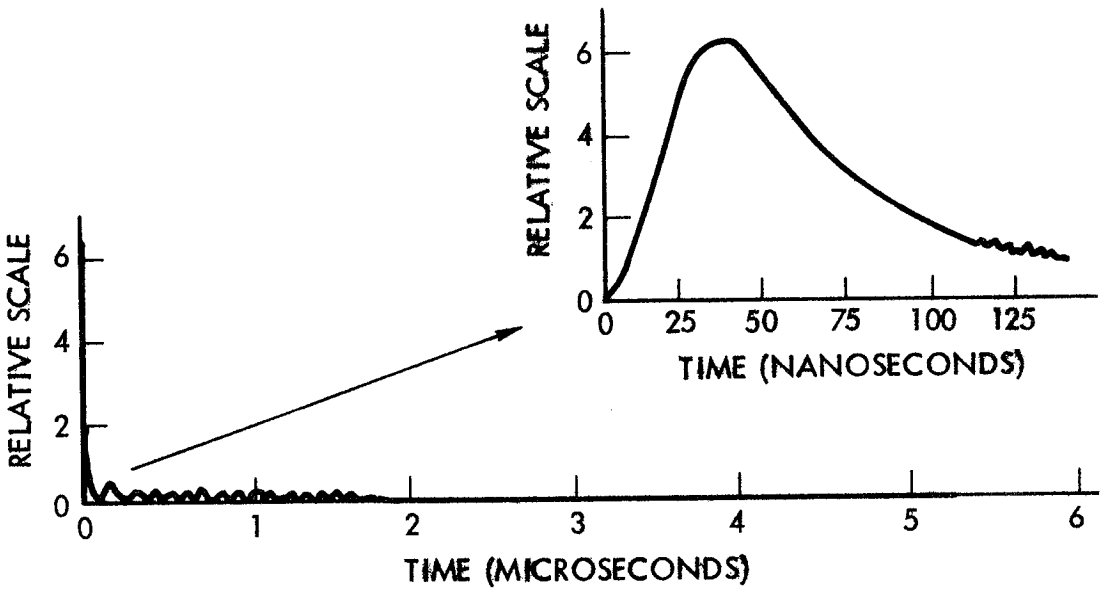

Figure 2a

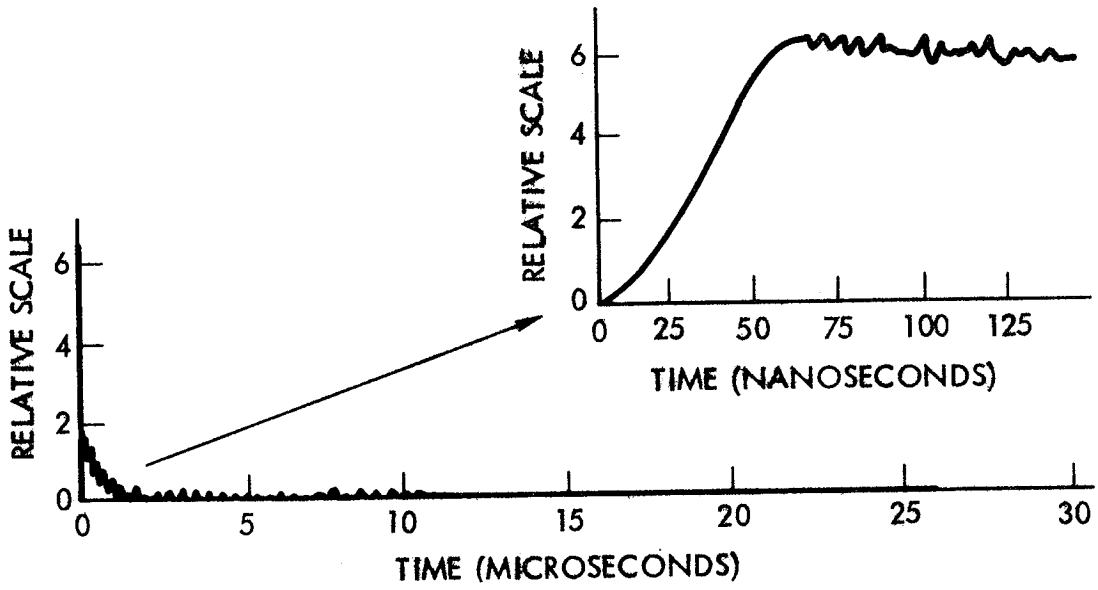

Figure 2b

Figure 2. Intensity-time behavior of impact light flash on a 800 Å thick gold foil with "fast" particles (Figure 2a) and "slow" particles (Figure 2b).

target. The risetimes are identical, both about 25 nanoseconds. The decay times also appear to be the same, about 60 to 70 nanoseconds. The thick target signal has a long time constant signal added to the short pulse. This long duration signal is simply missing for impacts into the thin foil. This appears consistent with the radiating hot crater explanation. For thin foil impacts there would be very little hot mass left on the foil as the particle passed through and therefore very little blackbody radiation.

For the slow particles, the risetime is the same as the risetime from the thick target impact, however, the decay time is much shorter. Again this seems consistent with the blackbody radiation explanation. One would expect the surface-area-to-volume ratio to be much larger for the hot mass on the thin foil which would mean a shorter thermal time constant.

4. SPECTRAL DISTRIBUTION OF IMPACT LIGHT FLASH

We have measured the spectral-distribution of the impact light flash for two target materials, using iron particles at three different velocities (approximately 10, 20, and 30 km/sec). The two target materials were tantalum and tungsten. The experimental arrangement is sketched in Figure 3.

Velocity selected particles were allowed to strike the face of a target which was viewed simultaneously by two photomultiplier tubes (PMT). One PMT was a RCA 6199 which has a spectral response in the visible (S-11) and served as a control for the experiment. The other PMT was an EMI 6255 with an extended response in the ultra violet. The spectral sensitivity of this tube was calibrated at our facility and the relative response error was estimated to be less than $\pm$ 15%. A quartz window was used in the vacuum chamber. A cut-off filter and an interference filter was placed between the quartz window and the PMT. Signals from the two PMTs were displayed simultaneously on a dual beam oscilloscope and photographed for later analysis.

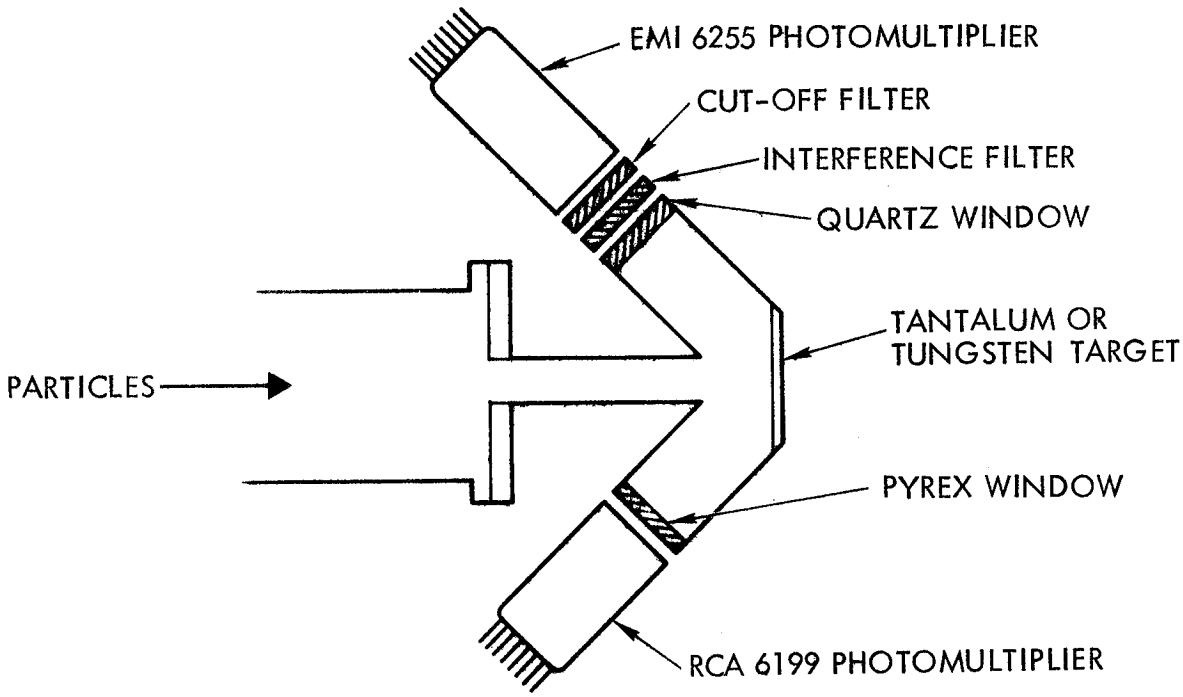

Figure 3. Block diagram of experiment to measure the spectral distribution of light from the impact light flash.

Two cut-off filters were used. An ultraviolet cut-off filter, Corning Glass CS 3-74 was used when making measurements in the visible region of the spectrum, and a visible cut-off filter, Corning Glass CS 7-54, was used when making measurements in the ultraviolet. Narrow pass-band interference filters (made by Optics Technology, Inc.) were used to further limit the region of the spectrum to be measured. Since the spectrum to be measured extended into the ultra-violet wavelengths, a quartz vacuum window was required for the EMI 6255. An ordinary glass window is opaque to ultra-violet radiation and would have seriously limited the sensitivity in this wavelength region. Quartz is transparent to visible and ultra-violet wavelengths down to about 2100 Å. At this wavelength transmission through one millimeter thick quartz is still above 90%.

For each of the three velocity ranges, between 5 and 10 particles were recorded for each of the fourteen interference filters. This was done for both target materials so that, all told, data from 400 to 800 particles were analyzed. The wavelength range covered was from 2400 Å to about 5600 Å.

If the sensitivity of the PMT as a function of wavelength λ is given by $S(\lambda)$, the transmission of the cut-off filter by $C(\lambda)$ and the transmission of the narrow pass-band filter by $g(\lambda)$, then the current at the anode of the PMT is given by

$$i = K \int_{\lambda} I(\lambda)\ S(\lambda)\ C(\lambda)\ g(\lambda)\ d\lambda \qquad (4\text{-}1)$$

where $I(\lambda)$ is the intensity distribution of the light flash and K is a constant involving solid angle and tube gain.

This integral cannot be evaluated without knowledge of $I(\lambda)$, the object of the experiment. Therefore we assume $I(\lambda)$ is varying slowly enough that it may be represented by some average value $\bar{I}$ over the wavelength region covered

by any given interference filter. Then, if the region covered by the interference filter is λ_1 to λ_2, we have

$$i = K \bar{I} \int_{\lambda_1}^{\lambda_2} S(\lambda)\ C(\lambda)\ g(\lambda)\ d\lambda \quad . \tag{4-2}$$

This integral was evaluated numerically for all of the interference filter, cut-off filter, PMT combinations. Since we are interested only in the relative intensity from one wavelength band to the next, the constant K drops out, and the final relative intensity curves are a plot of the current at each wavelength interval, divided by the value of the integral in Equation (4-2) over that wavelength interval. The result was then normalized to the total light output in the visible, as measured by the RCA 6199 photomultiplier tube.

Although the viewing angle of the PMTs can affect the current output from a given impact, we have assumed that when averaged over a number of particles, circular symmetry can be realized about the impact axis. Therefore, with both PMTs viewing the target at 45°, on the average they will receive equal radiation intensity even though they are viewing the target from opposite sides.

The results for the tantalum target are shown in Figure 4, and those for the Tungsten target in Figure 5. In each figure three curves are shown representing the results from the three velocity ranges.

It is difficult to say much about these curves. They exhibit a fair degree of internal consistency - that is, the curves for the three velocity ranges are all about the same. One might expect that the impact light flash would have a spectrum approximating a black body and characterized by some temperature and that the peak intensity would occur at shorter wavelengths as the particle energy increased. Therefore, since almost ten times as much energy per atom is carried by the 30 km/sec particle compared to the 10 km/sec

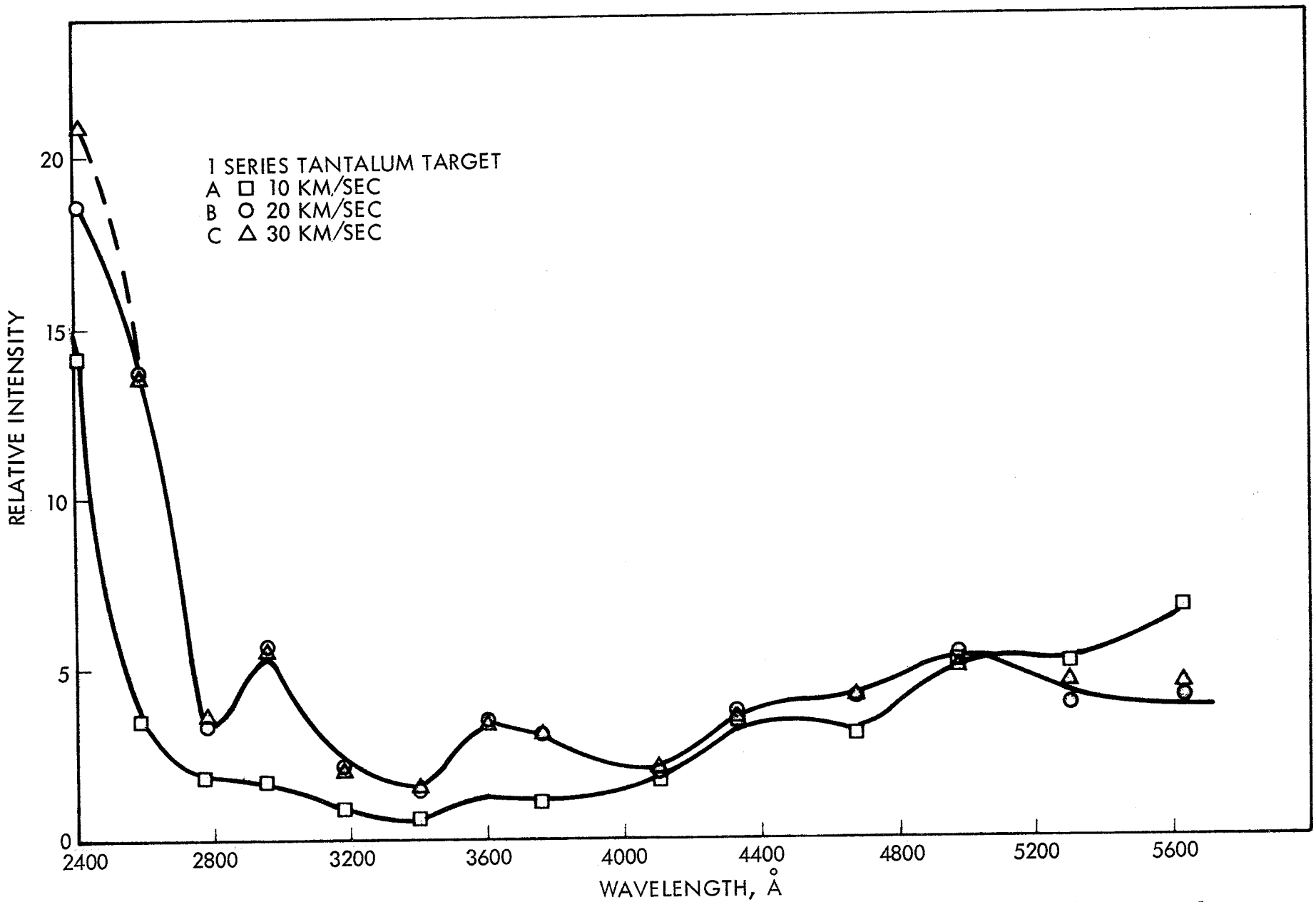

Figure 4. Spectral distribution of impact light flash from iron particles impacting a tantalum target. Results are shown for three different particle velocity ranges.

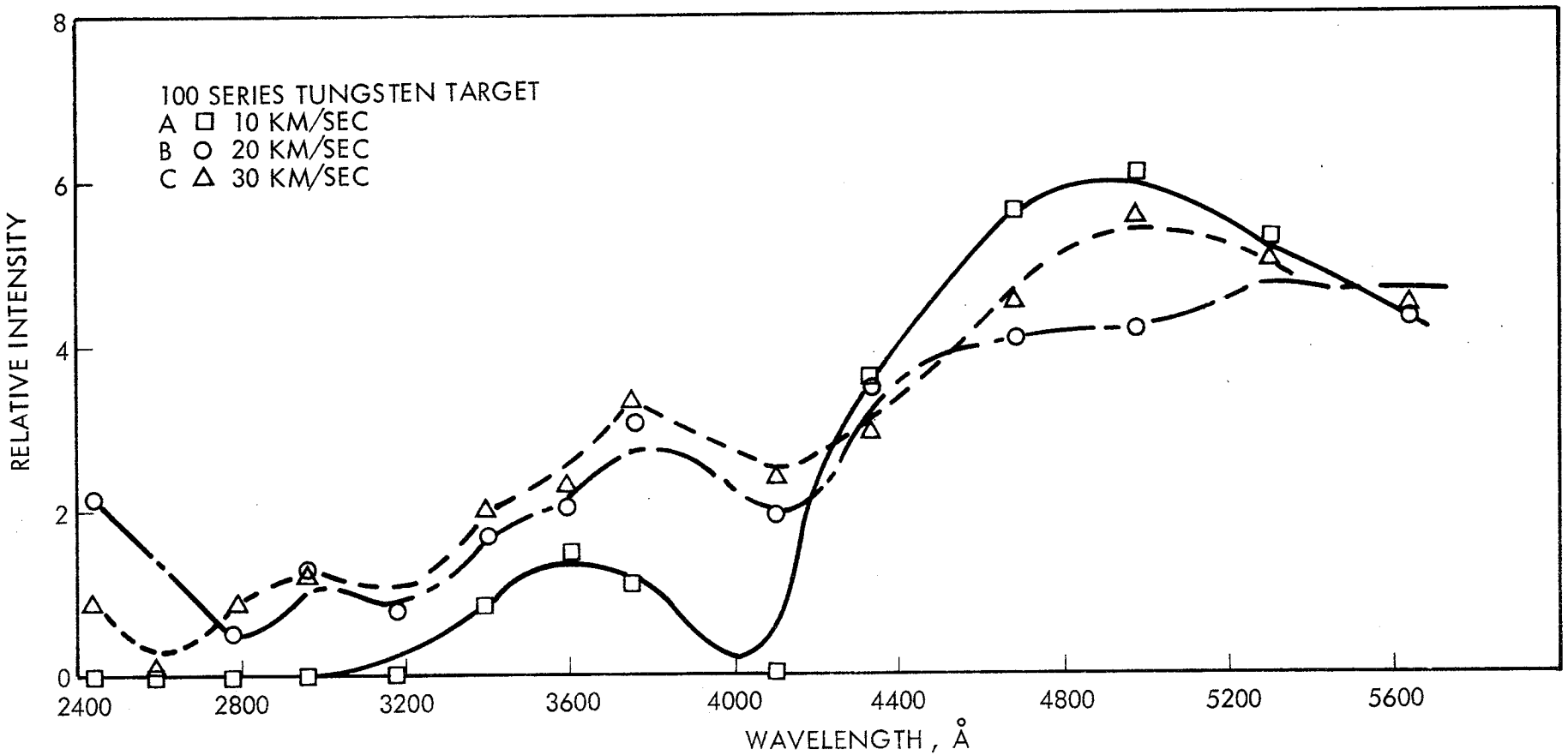

Figure 5. Spectral distribution of impact light flash from iron particles impacting a tungsten target. Results are shown for three different particle velocity ranges.

particle, the temperature should be higher and the three peaks would show a consistent movement toward the shorter wavelengths. Apparently this did not happen and consequently the curves are probably not simply black body curves. Instead they resemble more the atomic line spectra from heavy atoms (which normally contain many lines) which have been smoothed and averaged by the measuring process. If they are line spectra rather than black body spectra, one would not expect to find a peak which shifted smoothly with incoming particle energy.

It would appear, then that these may be averaged and smoothed line spectra (from which no inference to plasma temperature should be drawn) and that the spectra are characteristic of the target material rather than the particle material. This last conclusion is drawn because the curves for the two materials differ markedly. If the dominant contribution was from the iron in the particle the curves should be much more similar.

An alternative possibility is that the curves are composites of line spectra and continuum radiation. We are led to speculate on this possibility from the intensity-time characteristics discussed in the previous section. However, we can only speculate since the character of the curves do not permit a definite conclusion to be drawn.

In retrospect, it appears that a more definitive experiment could be conducted by recording, not the peak current from the PMTs, but the current at each wavelength as a function of time and normalizing to the total at each time interval of interest. It is quite possible that this technique would separate the radiation previously assumed to be from the impact plasma and that occurring later, presumably from blackbody radiation.

5. THIN FILM CAPACITORS

We evaluated the performance of thin-film capacitor micro-particle detectors. The detectors we chose were manufactured at TRW, were 1" by 1"

in area, with a capacitance of about 60 x 10^{-9} farads. They consisted of a 200 to 300 Å thick Al film on both sides with a dielectric between them of a polyvinyl chloride about 500 Å thick. The breakdown voltage was about 25 volts.

These capacitors detect the passage of a hypervelocity particle through the capacitor. The passage of the particle creates a momentary short circuit of the front Al film to the back Al film. Because of the short circuit the voltage across the capacitor falls and this is the signal indicating the particle impact. The current flowing from one plate to the other will (hopefully) burn out the short circuit and restore the capacitor to its original condition, at which point the voltage across the capacitor builds up again.

The functioning of these detectors depends on several factors. First of all, the particle must short out the capacitor as it goes through, otherwise there is no signal. Also, the magnitude of the signal generated depends on when the short is burned out. If this happens very quickly, the voltage across the capacitor will fall only slightly. In addition, the voltage across the capacitor cannot be too low or the short will not burn out at all, leaving a permanently shorted capacitor. However, higher voltages create a noise problem because there is an irregular leakage current. All of these problems are compounded by attempting to go to very thin capacitors.

The detectors are very difficult to use. They are very fragile and two of them were ruined through mishandling before they could be tested. In use it was common for them to develop a relatively low resistance leakage path which would lower considerably the voltage across the capacitor because it was connected to the power supply through an isolating resistor of 500 k ohm. When this happens, the accepted cure is to apply briefly the higher voltage without the isolating resistor, in an attempt to burn out the leakage paths. Sometimes this worked and sometimes it would permanently short the capacitor.

In spite of these problems we managed to test five different detectors with voltages across them ranging from three to fifteen volts. The largest signal observed (due to a particle passage) was about 0.05 volts. However there was

no consistency in the behavior. A few particles produced small signals but most did not (or else signals too small to observe), at all capacitor voltages.

The half-life of the detectors was short, about one-half hour, because of the developing leakage and subsequent burn out attempts mentioned above. After three had failed while attempting to cure low resistance leakages which developed, the experiment was abandoned.

If an evaluation is desired, this particular set of detectors was unsatisfactory. However, it is difficult to extrapolate these results to any other kind of capacitor detectors, or even to the same kind of detectors from a different batch. We believe, although there is not much evidence to back it up, that these capacitors were too thin and that if they had been two or three times as thick we would have had less problems. Of course thicker capacitors require larger particles to penetrate and are more likely to break up the particle.

6. MICROPHONE SENSORS

6.1 CHOICE OF DETECTOR TYPES

Two basic types of microphone sensors have been used on spacecraft for the detection of micrometeoroid impacts. The first of these utilizes a piezoelectric type crystal transducer generally fastened to some type of "sounding board" arrangement to increase the impact sensitive area of the detector. The second type is a capacitance microphone which, as the name implies, is essentially a charged capacitor having one fixed plate placed in close proximity to a movable one generally formed by a very thin membrane stretched taut in "drum head" fashion.

Time would not permit a study of both sensor types and, as a result, the capacitor microphone was chosen over the piezoelectric type. This was done for two principal reasons. First, the capacitor microphone is the more

sensitive one and it vibrates at one simple frequency which allows filtering networks to be applied thereby improving the signal-to-noise ratio. Second, the piezoelectric type transducer response would undoubtedly be dependent upon the particular "sounding board" geometry used.

6.2 EXPERIMENTAL ARRANGEMENT

The Langley Research Center's Microparticle Linear Accelerator was used for the microphone response studies because of the much higher particle momentum at any given velocity. A block diagram of the accelerator system is shown in Figure 6. Particles are introduced into the Van de Graaff (VDG) generator which supplies the initial energy necessary for injection into the linear accelerator (linac). A velocity selection system was placed at the output end of the VDG generator which allowed a small input velocity range to be selected before injection into the linac. Therefore, at any given time, the particles impacting the microphone sensor would be restricted to some narrow velocity range thus insuring that the output signal would remain within some relatively narrow limits.

A particle having the prescribed velocity requirements is detected by the sensors at the input end of the linac which then activates the system and causes accelerating voltages to be applied to the linac structure in the correct time relationship for that particular particle. The frequency generating electronics provide an output pulse as the accelerated particle exits from the linac. This provides a ready means for oscilloscope triggering and display of the particle as it passes through the particle charge detector before impacting on the microphone sensor. A second sweep is also triggered which displays the signal from the microphone as the particle impacts upon it.

The particle charge (measured from the particle charge detector) together with the particle velocity (provided by the linac frequency generating electronics) and the total accelerating voltage provide the required data for calculation of particle momentum for each impacting particle. The momentum of

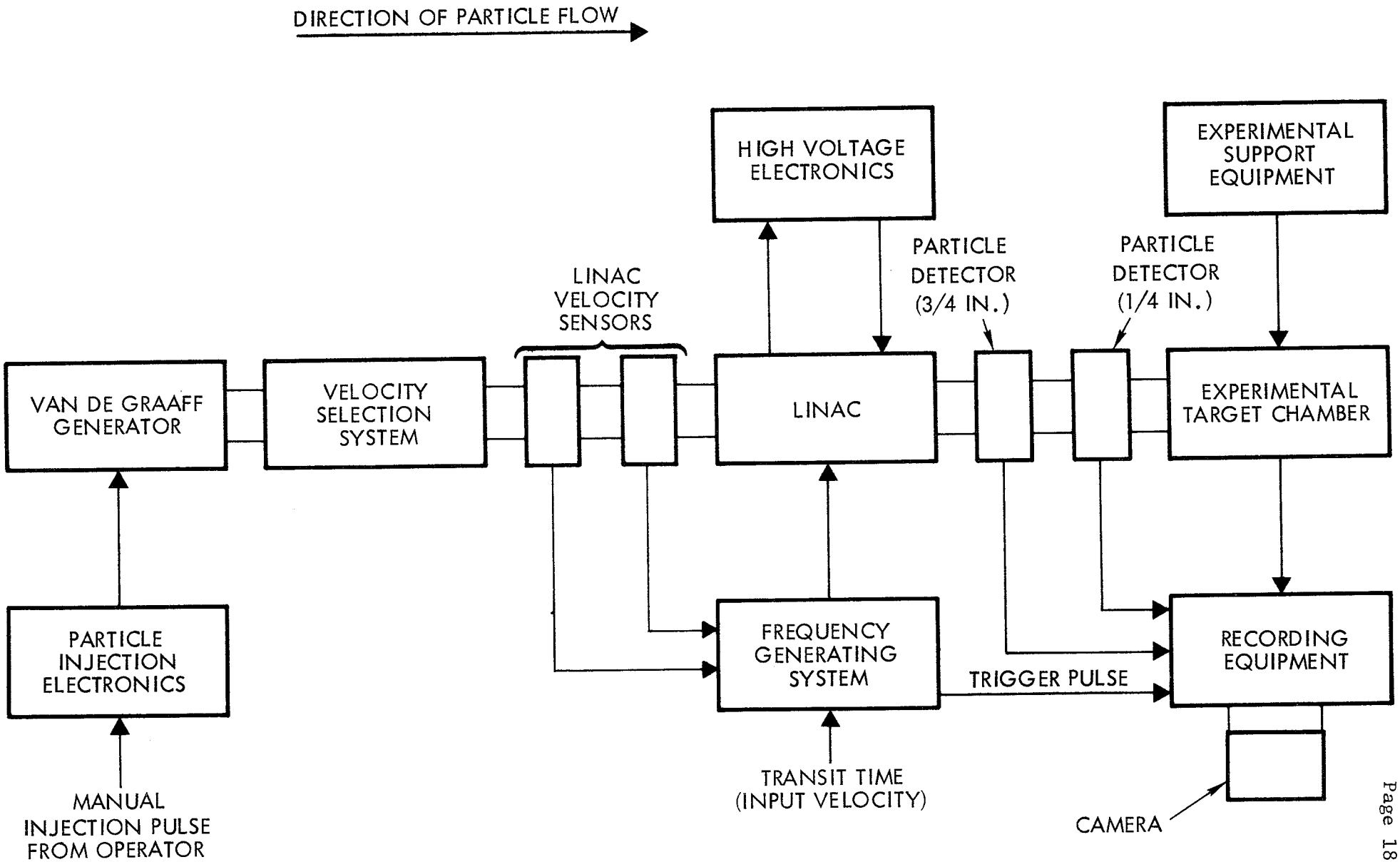

Figure 6. Block diagram of linear accelerator and experimental arrangement to measure the response of a capacitor microphone particle detector.

the impacting particle may be calculated in the following manner. A charged particle with charge Q, mass m, and accelerated through a potential Va will have a velocity v defined by the following equation which assumes conservation of energy and equates the final kinetic energy to the initial potential energy.

$$\frac{1}{2} m v^2 = Q\ Va \tag{6-1}$$

The particle mass is then given by

$$m = \frac{2\ Q\ V_a}{v^2} \tag{6-2}$$

The momentum is given by

$$mv = \frac{2\ Q\ V_a}{v} \tag{6-3}$$

When using the linac, as will be explained later, the output velocity v_o will differ, in general, from the velocity used in equation 6-2 for the mass calculation. The momentum of the impacting particle is found from the product of the mass (eq. 6-2) and the output velocity v_o. The particle charge in the above equations is found by allowing the particle to pass through a charge detector[6] just prior to impact on the target microphone. The charge on the particle is found from the amplitude of the output pulse and the particle velocity may be determined from the known length of the detector and the particle transit time (output pulse length).

Particles exiting from the linac may be grouped in two categories; those that are "in phase" and a few which are "out of phase". In this case "in phase" refers to particles which have remained in synchronism with the linac switching waveform and has been accelerated through the full potential available from the linac. The "out-of-phase" particles are those that have lost synchronism in the final stages of acceleration, and consequently the net

accelerating voltage is a few hundred kilovolts less than the expected value. Because of the slight variation from the expected output energy, the input velocity and the injection voltage are used in all mass calculations.

The linac frequency generating electronics displays the particle transit time across a distance of 128 cm to an accuracy of better than 1%. The input velocity is therefore also known to better than 1%. The output velocity of any particle is equal to the input velocity times the square root of the total accelerating voltage-to-injection voltage ratio. For those particles that are "in phase", the total accelerating voltage-to-injection voltage ratio is at the design value, therefore the output velocity-to-input velocity ratio will be a constant for all such particles and equal to 2.6 for this machine.

The phase position of the particle as it exits the linac may be determined from each piece of recorded output data. For those particles that are in phase the output velocity is found quite accurately from the input velocity. For the few particles which are out of phase the output velocity must be determined from the output particle detector. This will be somewhat less accurate because of the shorter flight path over which the transit time is being measured. The output velocity will be known to an accuracy of better than 5% in all cases. For additional information on particle phase motion or the microparticle accelerator in general see Reference 2.

The capacitor microphone used in this experiment is a one-inch diameter model with a stainless steel membrane approximately 5 microns thick. This particular sensor has a resonant frequency of about 3200 Hertz and a Q of several hundred. The signal and bias leads for the sensor were made from #36 gauge magnet wire and the microphone assembly was suspended from rubber bands in the vacuum housing to provide the required acoustical decoupling from the laboratory environment.

A boot-strapped source follower utilizing a 2N4416 field effect transistor was used as the input stage of the microphone amplifier. The input source

follower was followed by a broadband amplifier having a selectable gain of 1, 10, or 100. The output of this amplifier was brought out through a line driver for direct broadband observation of the microphone signal and was also fed into a tunable LC filter with a provision made for varying the filter Q from about 10 to a maximum of 200. A schematic of the amplifier and filter appears in Figure 7.

6.3 RESULTS

Langley Research Center's Microparticle Linear Accelerator offers a significant increase in impact momentum at a given velocity over that available from electrostatic accelerators previously used for the study of microphone sensor characteristics. In a charged particle accelerator, utilizing charging techniques which charge particles to essentially a constant surface electrical field strength, it can be shown that the radius of accelerated particles varies directly with the accelerating voltage, at any given velocity. Thus the mass, and consequently the momentum, varies directly as the cube of the accelerating voltage. The higher accelerating voltage provided by the linac yields a remarkable increase in particle impact momentum, even when operated at the conservative seven million volts used in this experiment. At this voltage the particle momentum is two orders of magnitude greater than that available from the 1.5 million volt accelerator previously used by this organization.

The much larger momentum available has resulted in what appears to be a very worthwhile extension of the response characteristic of one type of microphone sensor to higher velocities. This is of particular significance since this extension to higher velocities is into a region where the response characteristics have definitely changed from that at lower velocities. A plot of the peak-to-peak filtered microphone output response, normalized to impacting particle momentum, versus velocity is shown in Figure 8. This is a plot of the raw data without benefit of the exclusion of widely scattered points which can be justified by statistical arguments.

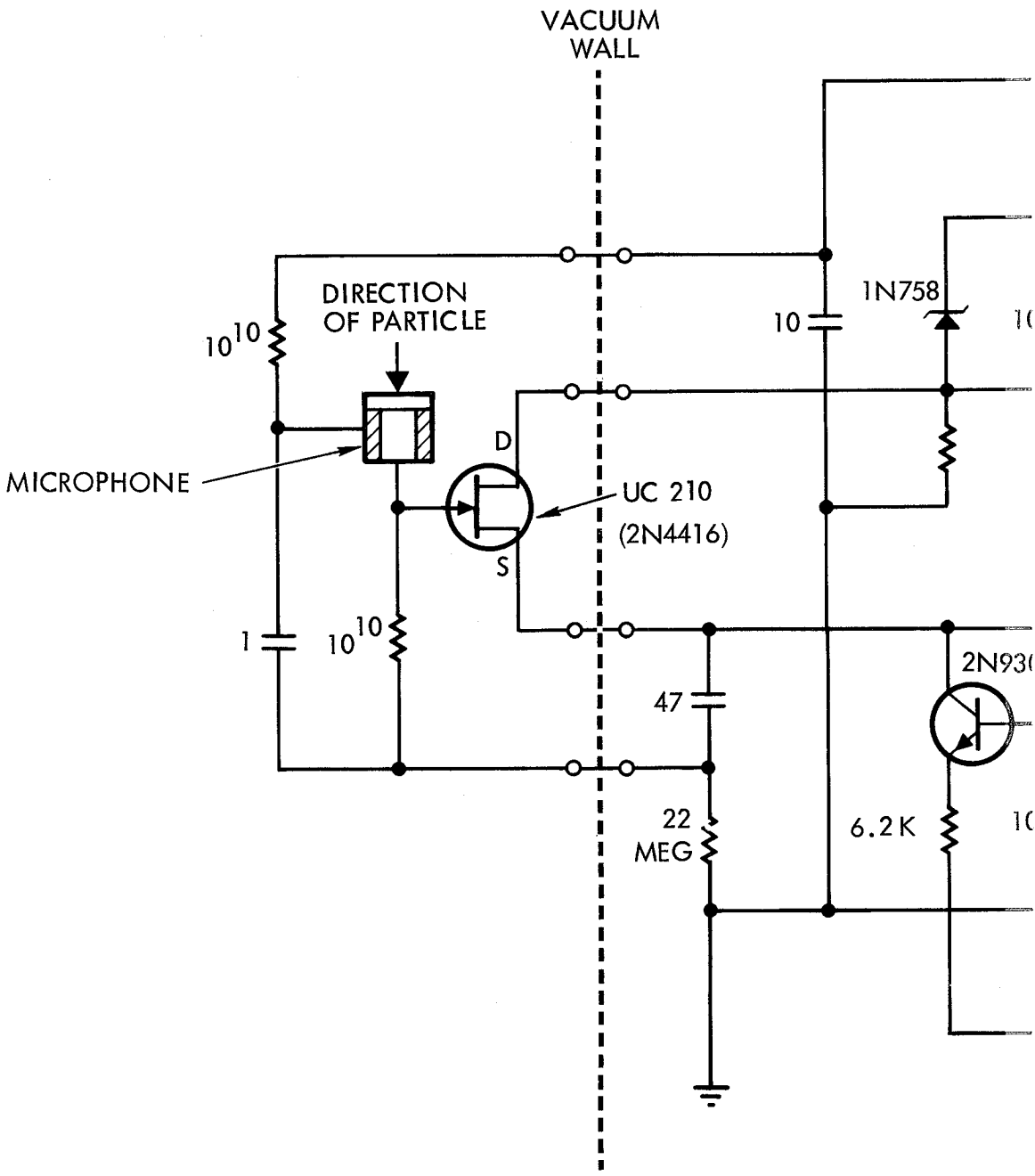

CAPACITOR VALUES ARE IN μfd,
RESISTOR VALUES ARE IN OHMS

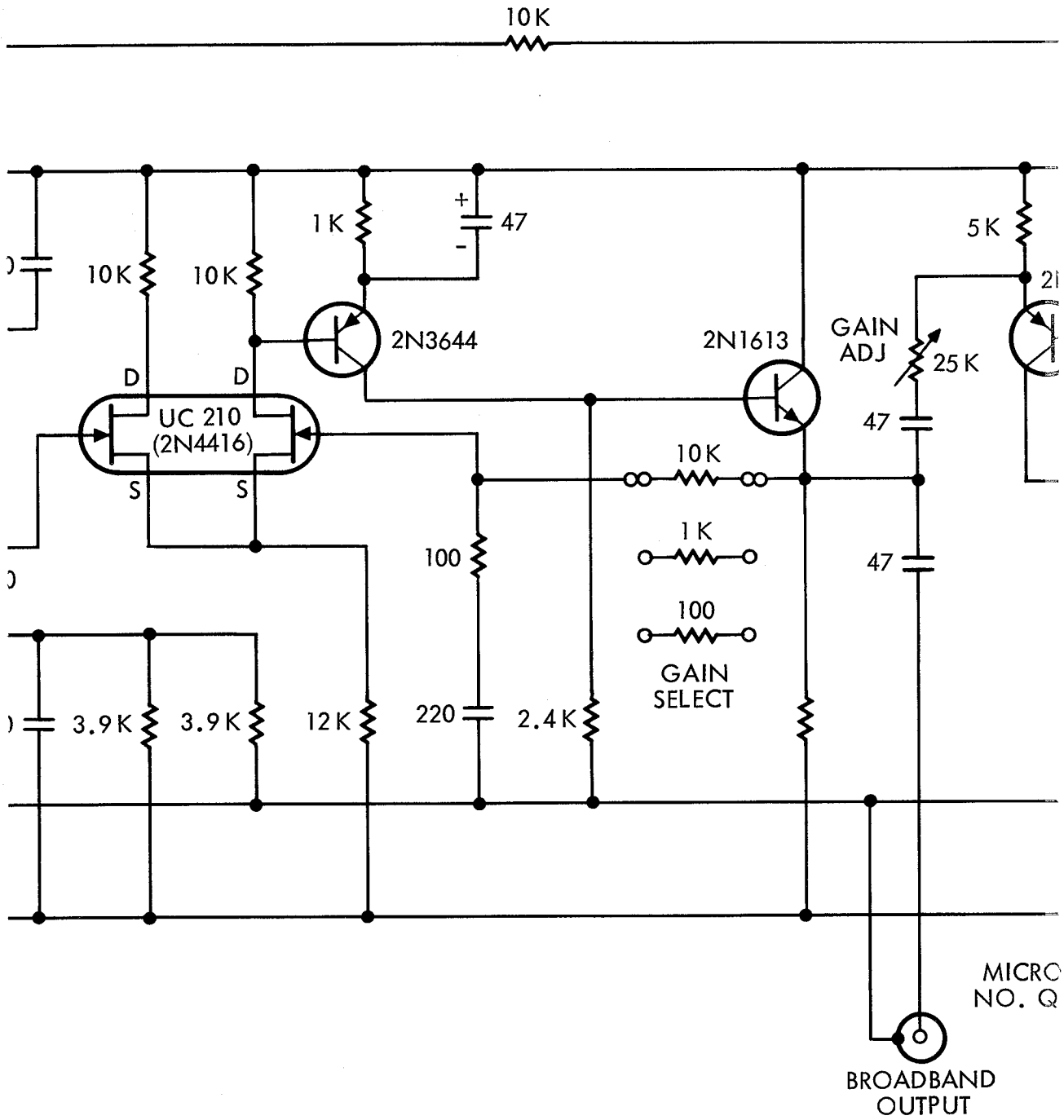
10K
10K
10K
1K
+
47
-
2N3644
2N1613
5K
GAIN
ADJ
25K
D
D
UC 210
(2N4416)
S
S
47
10K
1K
100
47
100
GAIN
SELECT
3.9K
3.9K
12K
220
2.4K
MICRO
NO. Q
BROADBAND
OUTPUT

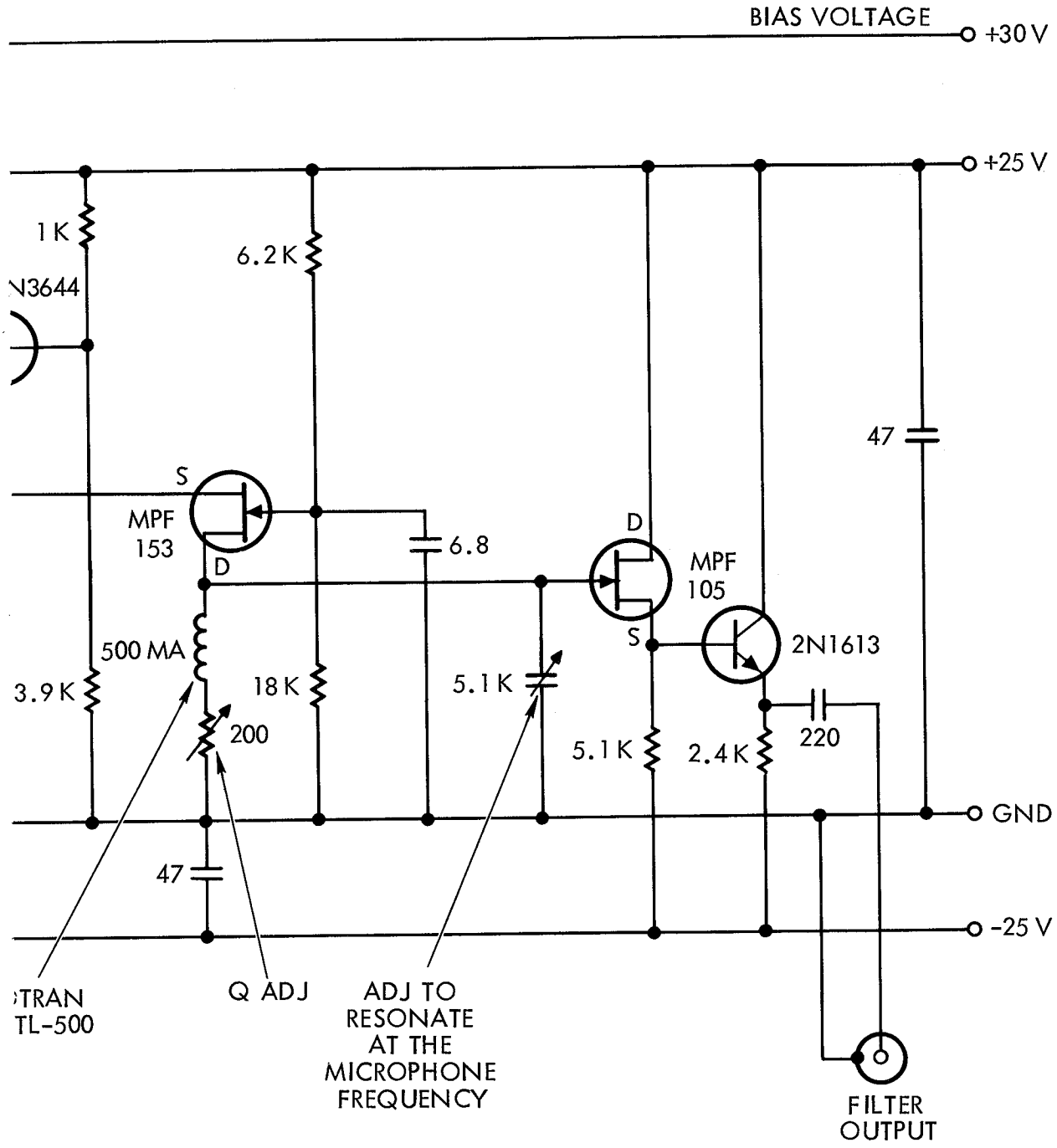
BIAS VOLTAGE
+30 V
+25 V
1 K
N3644
6.2 K
47
S
MPF
153
D
6.8
D
MPF
105
S
2N1613
500 MA
3.9 K
18 K
200
5.1 K
5.1 K
2.4 K
220
GND
47
-25 V
TRAN
TL-500
Q ADJ
ADJ TO
RESONATE
AT THE
MICROPHONE
FREQUENCY
FILTER
OUTPUT

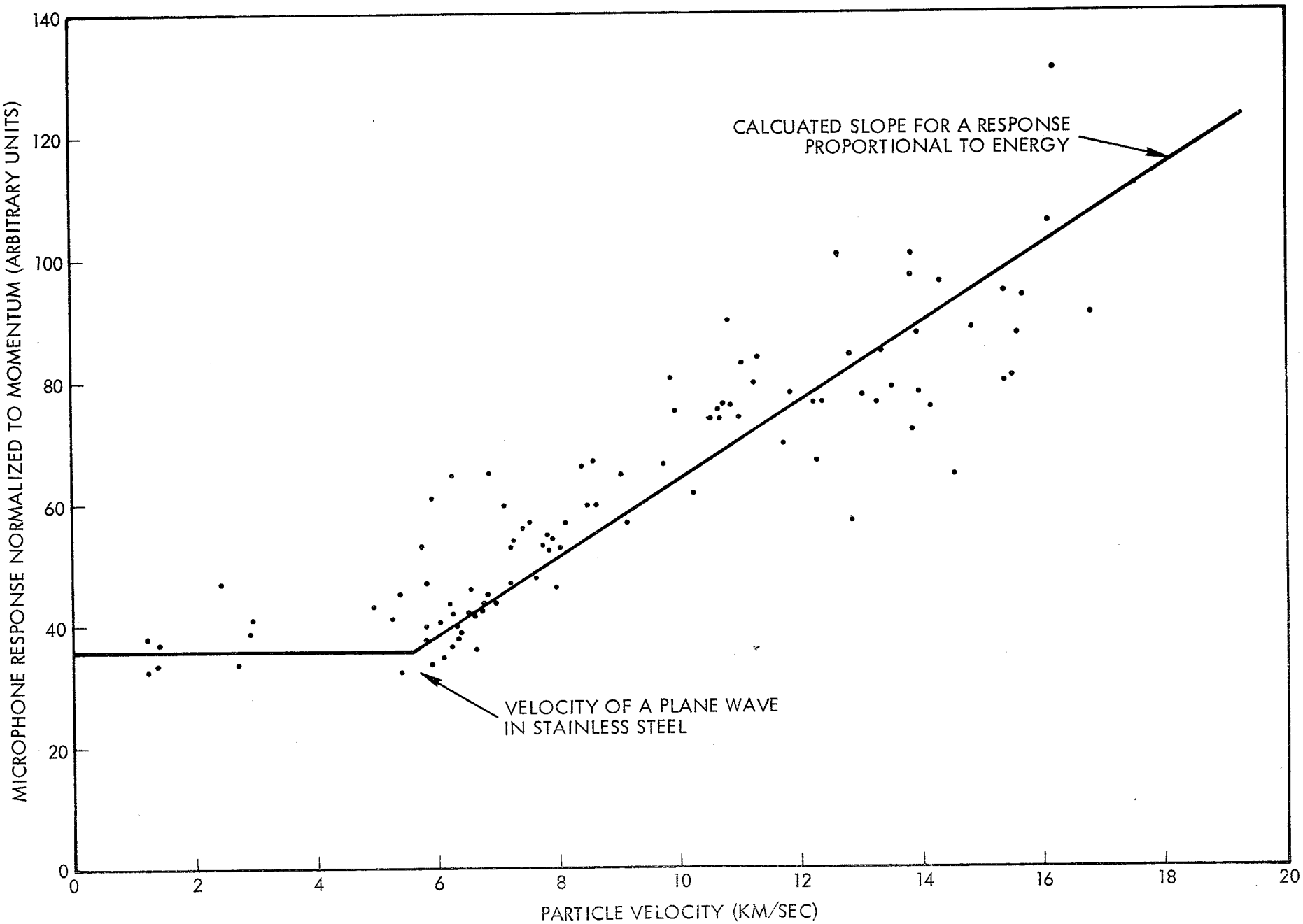

Figure 8. Output signal from the capacitor microphone, normalized to incoming particle momentum, as a function of impacting particle velocity.

Although only a small number of data points exist at the lower velocities (under 6 km/sec), it can be seen that this portion of the microphone response is essentially momentum dependent as exhibited by the flat response characteristics in this plot. This type of microphone is also known to have a low velocity momentum dependent output from work performed by this organization and others in the field. However, at about 6 km/sec, the sensor output response changes from a momentum dependence (first power of input velocity) to a response which closely approximates an energy dependence (second power of the input velocity). A least squares fit has not been attempted on these data; the line shown above 6 km/sec is that of a response characteristic which goes to zero velocity and whose slope is that calculated for a microphone response proportional to energy. The horizontal line below 6 km/sec approximates the momentum dependent characteristic at low velocities.

It is interesting to note that the two-piece linear curve is not a bad fit to the raw data. Furthermore, the breakpoint in the response characteristics appears at about 5.7 km/sec which is quite close to the propagation velocity of an acoustic wave in the impacted stainless steel membrane (velocity of a plane longitudinal wave in stainless steel is approximately 5.8 km/sec).

The data, as shown here, displays a considerable amount of scatter and further work is needed in reducing this scatter before attempting any additional refinement of the response characteristic. It is believed that the major portion of scatter is due to an error between the filter resonant frequency and that of the capacitor microphone. The first set of data taken on this sensor was done with a filter Q of approximately 200; however, frequency drift due to thermal changes caused such large errors that the data was not useable. The data shown here were taken with a filter Q of about 30 and an effort was made to keep the filter tuned to the microphone frequency. However, frequency drift with time was still noted thereby requiring frequent tuning of the filter to prevent an excessive voltage gain error. The use of temperature stable capacitors in the tuned circuit and a constant temperature sensor may therefore considerably improve the data.

The sensor response graphed in Figure 8 is essentially an integrated output response since the signal has been processed through a relatively high Q filter which "sums up" a large number of cycles to arrive at its final output level. Although an excellent signal-to-noise ratio was maintained with the filter, even at the maximum velocity, the instantaneous output signal upon impact would not have been measurable to as high a velocity due to the broadband response needed.

A typical instantaneous response from the microphone is shown in Figure 9-a together with a portion of the filter response on the lower sweep. Figure 9-b shows the broadband response on a slower sweep (upper trace) and the filter response on the lower trace. In Figure 9-c is shown the highest velocity particle recorded in this particular experiment; the upper trace is the signal produced as the particle travels through two position-charge detectors and the lower trace is the resultant microphone signal at a much slower sweep speed. This is an example of the signal-to-noise ratio still available at 17 km/sec. The 17.6 km/sec particle had an impact momentum of 4.6×10^{-7} dyne-sec. The noise level achieved in this experimental sensor system, in momentum units, was approximately 5×10^{-8} dyne-sec, which resulted in a 10 to 1 signal-to-noise level for the highest velocity particle in these data.

6.4 CONCLUSIONS

From the data obtained on this microphone sensor it is apparent that the momentum response characteristic obtained by "bead dropping" and other low velocity techniques cannot be extended to velocities above about 6 km/sec without introducing gross errors. Furthermore, at about 6 km/sec, the microphone response becomes essentially energy dependent up to the 17 km/sec range, although the scatter in the data obtained prevents a high degree of confidence in this type of simple response.

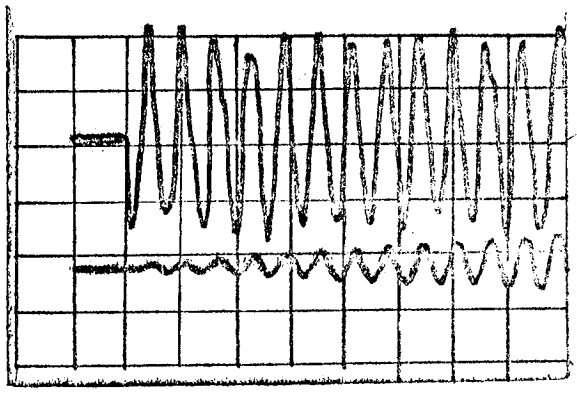

9-a

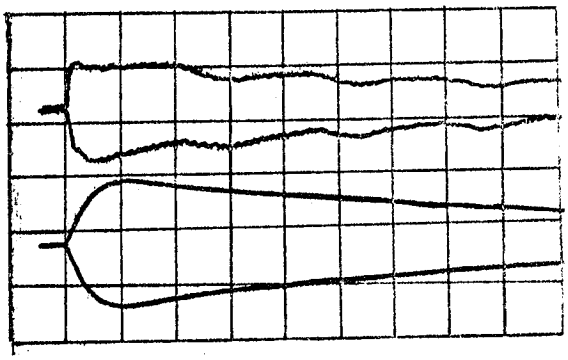

9-b

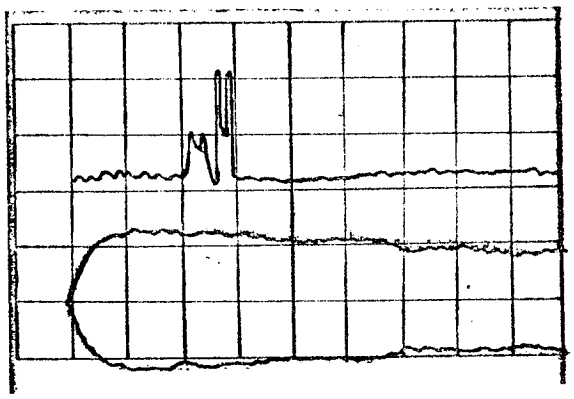

9-c

Figure 9. Oscillograms of microphone response.

a) Initial broadband microphone response (upper trace) and filter response (lower trace) at 500 microseconds per division horizontal scale.

b) Microphone broadband response (upper trace) and filter response (lower trace) at 50 milliseconds per division horizontal scale.

c) Filter response (lower trace) to highest velocity particle recorded - v = 17.6 km/sec, mv = 4.6×10^{-7} dyne-sec. Particle detectors are shown in upper trace.

7. CRATERING AND THIN-FILM PENETRATION

We have performed several experiments on cratering and/or thin-film penetration using particles from the linear accelerator. The experiments, described below, all had certain features in common. The targets were mounted in a micrometer-indexed movable target holder so that one section at a time could be moved in front of the beam aperture. A particle detector, mounted directly in front of the aperture, measured the particle parameters and also supplied x-y coordinates for locating the resultant craters.

Usually, only one particle was impacted in a given target area, but sometimes as many as two or three were tried. It proved quite easy to match the craters and particles when there were more than one because the particle sizes varied somewhat and so did the x-y coordinates. As usual, an oscilloscope photograph was taken for every particle and analyzed later.

After bombardment, the targets were first searched with an optical microscope. In general, craters or holes were very easy to locate. Some particularly small ones required as much as 15 minutes to find, but once located, were readily identifiable.

Once located optically and correlated with the appropriate particle, the craters were marked for subsequent location in the scanning electron microscope. The markings were usually a scratch made adjacent to the crater in the metal targets and small droplets of Silastic on the foil targets. Where more than one crater was present in an area, the markings were sufficiently different to be identified later in the electron microscope. Final measurements of craters and/or holes were made with a scanning electron microscope.

The scanning electron microscope operates by directing a high energy (about 24 kV), finely focused, electron beam onto the target. The beam has been condensed until it is about 100 Å in diameter. This beam is swept back and forth across a small area of the target in synchronism with the beam of a television picture tube.

Sitting off to one side of the target, and slightly above it, is a secondary electron detector. This detector operates at about 10 kV with respect to the target. As the primary beam moves across the face of the target, it produces secondary electrons which are drawn to the secondary electron detector. The signal from this detector is used to modulate the intensity of the television picture tube trace. The television screen is photographed and forms the final record. Because of the small currents in the primary beam, the secondary electron signal is small and a complete scan of an area may take from many seconds to minutes.

The net result is a picture of the sample which appears as though the observer were looking down the primary electron beam at a sample which is illuminated by a light positioned at the secondary electron detector. However, it must be kept in mind that what one is seeing is not scattered light but the secondary electron yield. Furthermore, the device is really only sensitive to changes in the secondary yield, rather than the DC level. If the secondary yield does not change as the primary beam is swept then that surface will appear featureless. This is apparent in the pictures of craters in stainless steel. The stainless steel targets were very carefully polished (to make the optical identification of the craters easier) and the surface appears completely dark in the pictures (see Figures 10 and 11).

This point is brough out because it quickly became apparent that we could not see the bottom of the craters. This was true even with the sample tilted at an angle. The microscopists did not understand why this should be, since at least some secondaries made as the beam scanned the crater bottom should escape.

In order to be sure the effect was not some defect in technique, we sent one of the samples to Sloan Research in Santa Barbara. This is a small consulting firm with a transmission electron microscope and also a scanning electron microscope. We have used them before and have great confidence in their technical ability. However, the pictures produced by Sloan were the same as

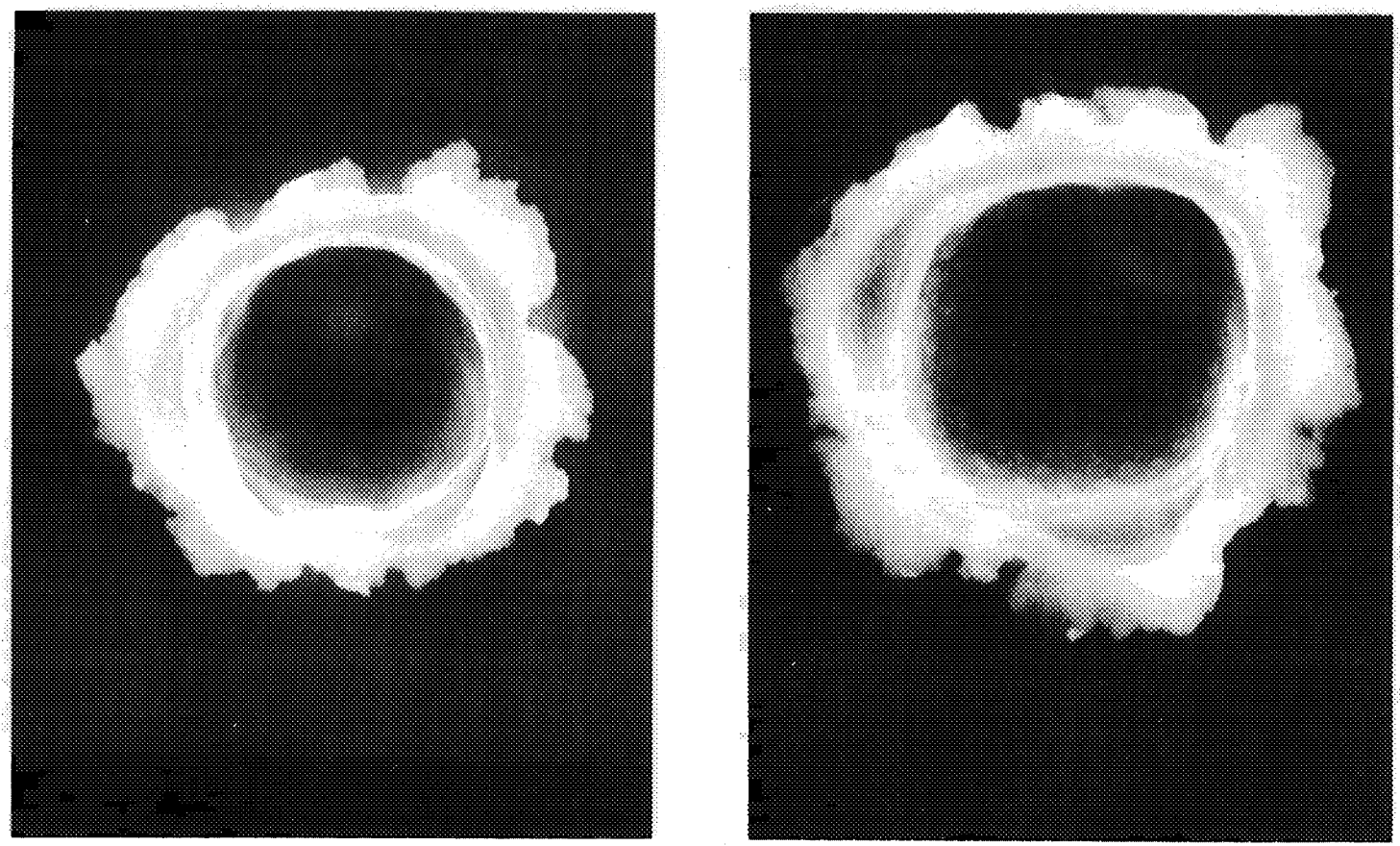

Target Material - 304 SS
Projectile - Iron
Diameter - 2.0 microns
Mass - 3.0×10^{-14} Kgm
Impact Velocity - 5.21 km/sec
Crater Diameter - 3.8 microns
Magnification - 10,000

Target Material - 304 SS
Projectile - Iron
Diameter - 2.8 microns
Mass - 9.3×10^{-14} Kgm
Impact Velocity - 3.91 km/sec
Crater Diameter - 4.7 microns
Magnification - 10,000

Figure 10. Photographs from scanning electron microscope of two craters in a 304 stainless steel target. Magnification, crater diameter and parameters of impacting iron particle given below each picture.

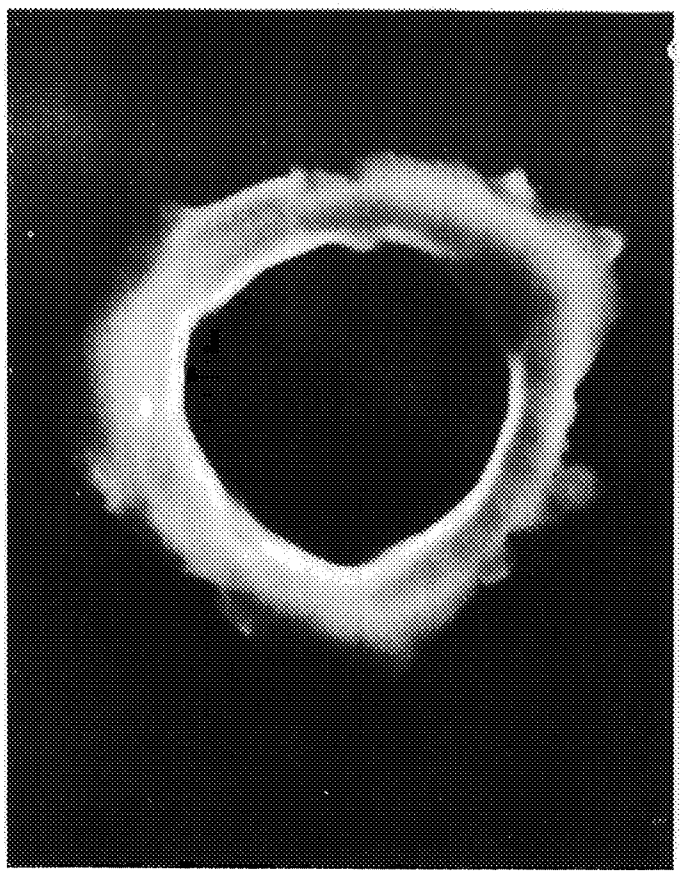

Target Material - 304 SS
Projectile - Iron
Diameter - .48 microns
Mass - 4.4×10^{-16} Kgm
Impact Velocity - 11.8 km/sec
Crater Diameter - 1.4 microns
Magnification - 30,000

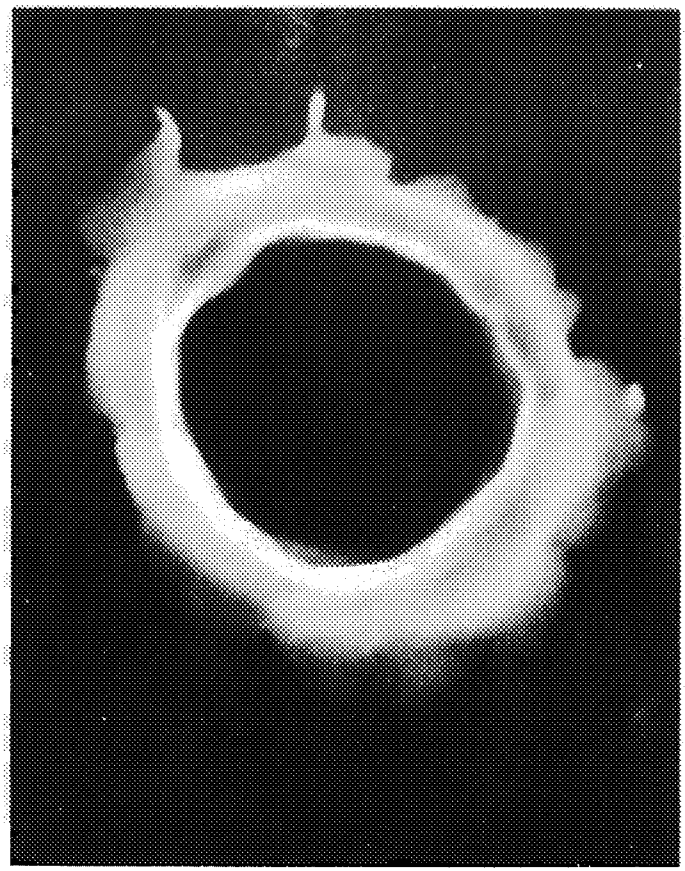

Target Material - 304 SS
Projectile - Iron
Diameter - .53 microns
Mass - 5.9×10^{-16} Kgm
Impact Velocity - 10.6 km/sec
Crater Diameter - 1.4 microns
Magnification - 30,000

Figure 11. Photographs from scanning electron microscope of two craters in a 304 stainless steel target. Magnification, crater diameter and parameters of impacting iron particle given below each picture.

those made by the TRW microscopists. The crater lip and crater diameter showed up with fine detail but there was no signal from the interior of the crater. This is annoying because it means that the crater depth cannot be measured.

Not enough time remained in the contract to solve this problem although we have some ideas about how to go about it. We did try evaporating a thin film of gold over one of the cratering samples in case some kind of surface oxcide effects were responsible. However, pictures of the gold covered craters were identical to the pictures of the same craters without the gold.

In retrospect, we should have selected a material other than gold. Gold is often chosen for thin conducting films because it coalesces into a uniform field at only about 50 Å thickness. Many materials however tend to form islands separated by bare spaces even at 200 Å or 300 Å, and this effect is enhanced by slight heating of the substrate. Ideally we would like islands about 400 Å in diameter separated by bare spots somewhat larger or about the same size. (The resolution of the microscope is about 250 Å.) Hopefully, the secondary yield from the islands of whatever material is evaporated would be different from the yield of the bare metal, thus supplying a signal to the television tube. Since we are interested in crater depths of about one micron (10,000 Å), the presence of 400 Å or 500 Å islands would not disturb the measurement very much. Figure 12 shows pictures of two of the smaller craters, made by higher velocity particles.

7.1 CRATERING DATA

Several targets of 304 stainless teel were prepared and bombarded at velocities up to about 16 km/sec. Examples of the scanning electron microscope pictures of the craters are shown in Figures 10 through 12. We also bombarded a stainless steel foil, 0.0002" thick, at lower velocites in an attempt to penetrate it with the larger particles. Although no penetration were observed in this foil, the data were used for crater diameter measurements. Examples of craters in the 0.0002" foil are shown in Figure 13 and 14.

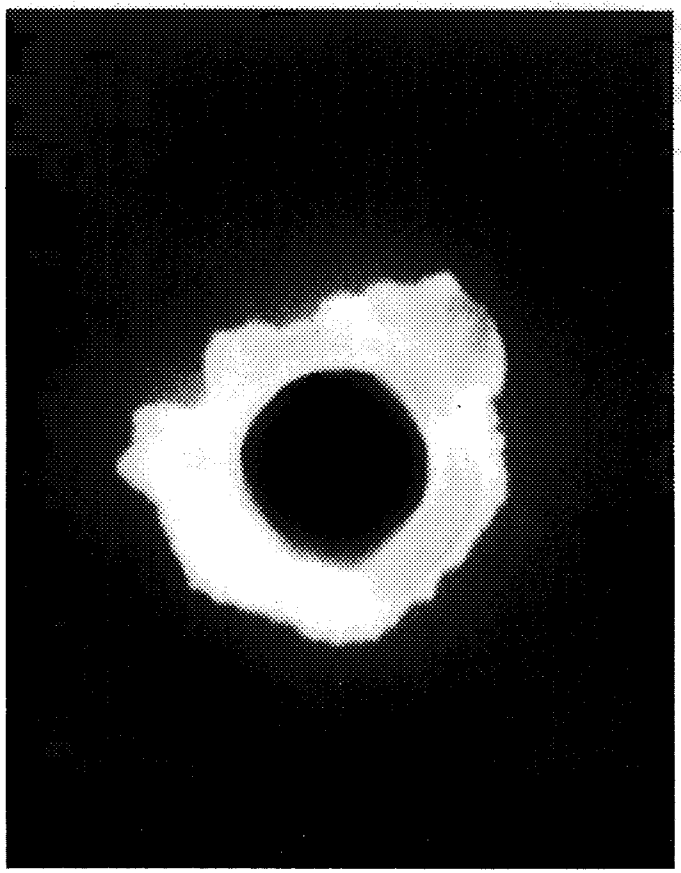

Target Material - 304 SS
Projectile - Iron
Diameter - .28 microns
Mass - 9.4×10^{-17} Kgm
Impact Velocity - 15.3 km/sec
Crater Diameter - .89 microns
Magnification - 30,000

Target Material - 304 SS
Projectile - Iron
Diameter - .37 microns
Mass - 2.0×10^{-16} Kgm
Impact Velocity - 15.5 km/sec
Crater Diameter - 1.1 microns
Magnification - 30,000

Figure 12. Photographs from scanning electron microscope of two craters in a 304 stainless steel target. Magnification, crater diameter and parameters of impacting iron particle given below each picture.

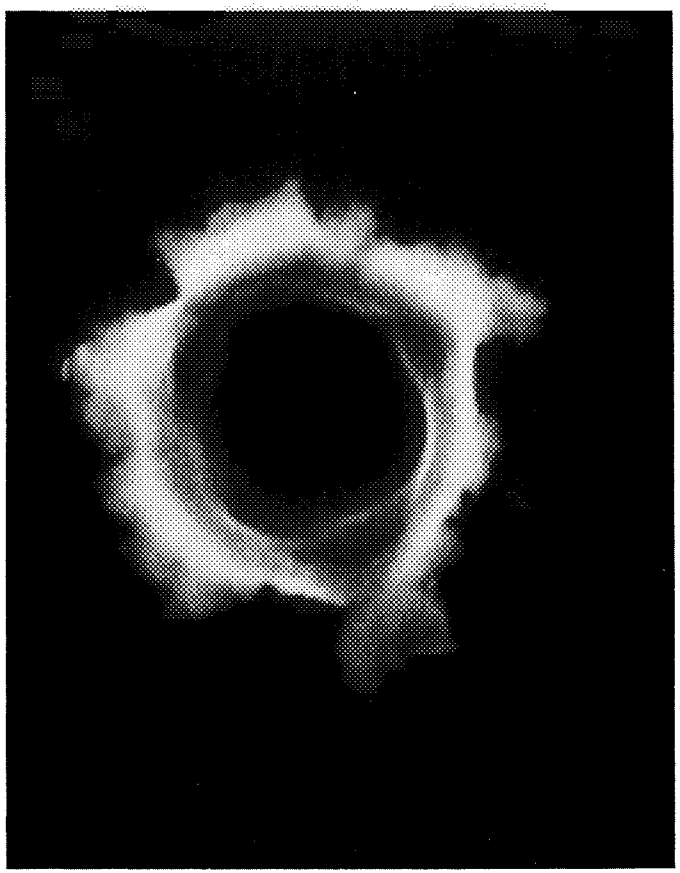

Target Material - .0002" SS Sheet
Projectile - Iron
Diameter - 2.3 microns
Mass - 4.9×10^{-14} Kgm
Impact Velocity - 3.73 km/sec
Crater Diameter - 3.6 microns
Magnification - 10,000

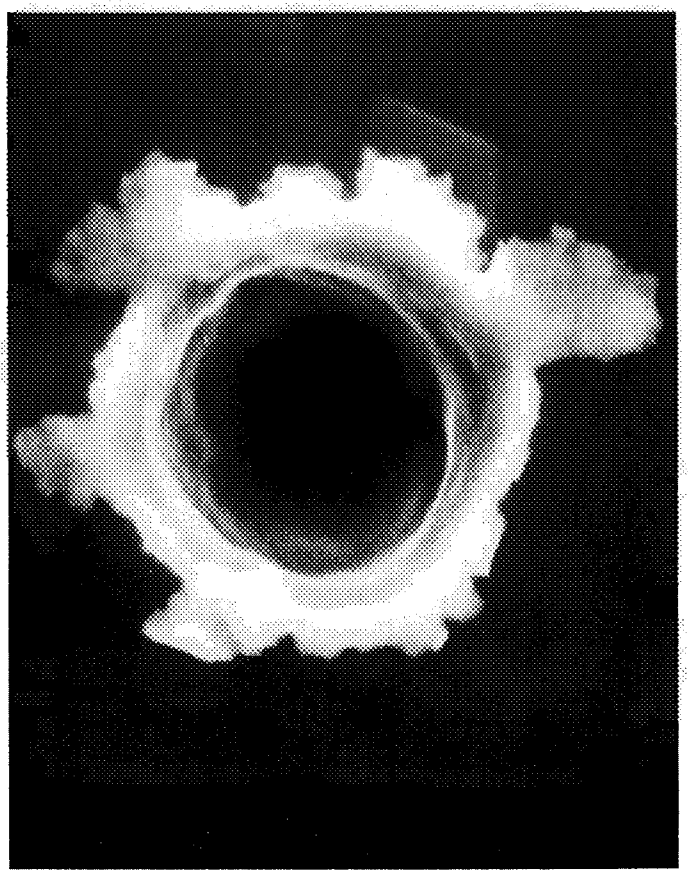

Target Material - .0002" SS Sheet
Projectile - Iron
Diameter - 2.1 microns
Mass - 3.9×10^{-14} Kgm
Impact Velocity - 4.68 km/sec
Crater Diameter - 3.8 microns
Magnification - 10,000

Figure 13. Photographs from scanning electron microscope of two craters a 0.0002" thick stainless steel foil. Magnification, crater diameter and parameters of impacting iron particle given below each picture.

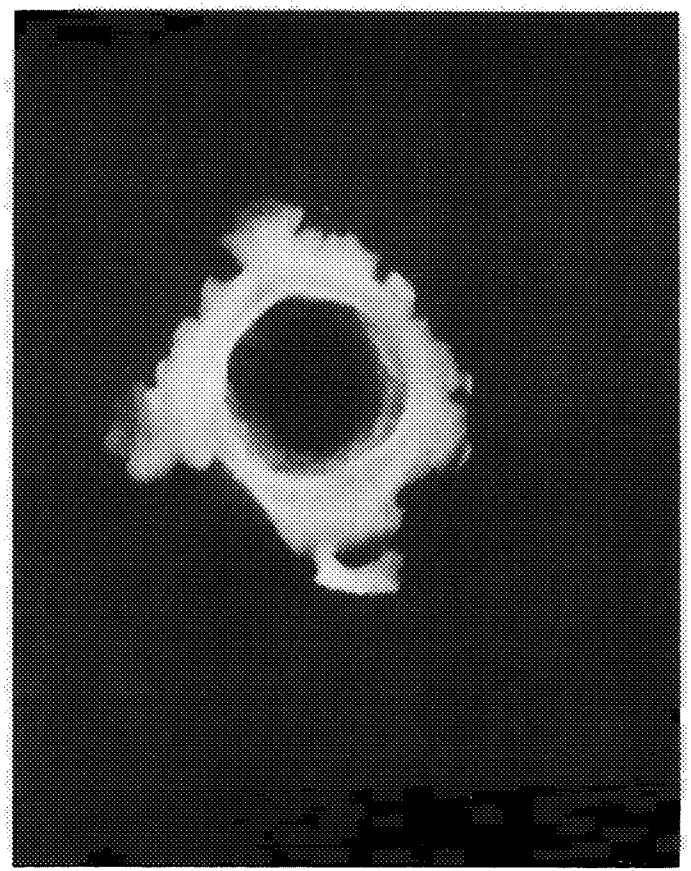

Target Material - .0002" SS Sheet
Projectile - Iron
Diameter - 1.04 microns
Mass - 4.6×10^{-15} Kgm
Impact Velocity - 7.15 km/sec
Crater Diameter - 2.5 microns
Magnification - 10,000

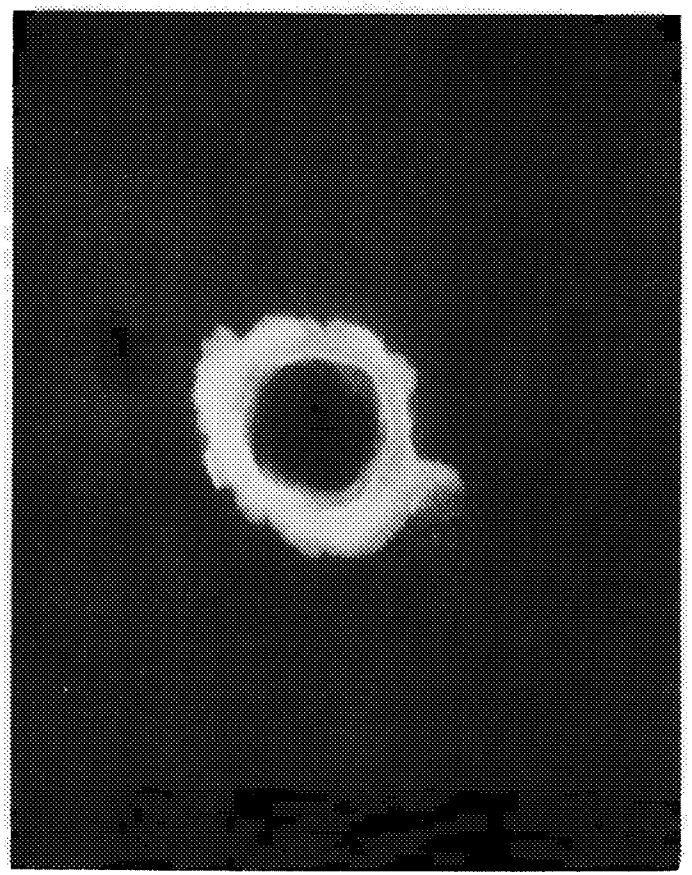

Target Material - .0002" SS Sheet
Projectile - Iron
Diameter - .85 microns
Mass - 2.5×10^{-15} Kgm
Impact Velocity - 7.17 km/sec
Crater Diameter - 2.0 microns
Magnification - 10,000

Figure 14. Photographs from scanning electron microscope of two craters a 0.0002" thick stainless steel foil. Magnification, crater diameter and parameters of impacting iron particle given below each picture.

The final data are given in Table I for the 304 SS target and Table II for the 0.002" steel foil. We have listed the particle velocity, radius and the crater radius (measured inside the crater lip) for each particle. Also listed is the ratio of crater diameter to particle diameter (D/d). This quantity (D/d) is plotted as a function of velocity in Figure 15.

Data from both the solid target and the foil are shown in Figure 15 with different symbols to distinguish them. The data appear to be very good with only a small scatter. These data should prove to be helpful in determining the projectile size effect on cratering for this material as was done recently for aluminum.[7] For soft aluminum into aluminum impacts at about 8 km/sec, the D/d ratio has been found to be about 3 for one micron size range particles,[8] while data for one millimeter to one centimeter projectiles yield a D/d ratio of 5 to 6 at the same velocity.[7] The D/d ratio for iron into stainless steel is about 2.5 at 8 km/sec (for one micron size range particles) compared to a D/d ratio of about 3 for similar aluminum to aluminum impacts. Assuming similar cratering ratios between steel and aluminum at the one centimeter size range, then the projectile size scaling effect for cratering would also be evident in this material.

7.2 THIN FILM PENETRATIONS

Two different foils were used for the penetration experiments. Both were nickel, one was 1.8 microns thick and the other was 1.27 microns thick. Ideally, an experiment of this kind should be designed so that some particles penetrate and some do not. This turned out to be the case for the 1.8 micron foil experiment, but the 1.27 micron foil was penetrated by all the particles, with penetrations recorded up to 15.5 km/sec. In retrospect, it would appear that we should have lowered the accelerator energy for the thin foil.

However the data is still good and is consistent. In Figure 16 we have plotted the results for the 1.8 micron foil as particle diameter versus particle velocity. The solid points are particles which penetrated the foil

TABLE I - Cratering Results from Iron Particles Impacting a 304 Stainless Steel Target

Particle Velocity (km/sec)	Particle Diameter (microns)	Crater Diameter (microns)	$\frac{\text{Crater Diameter}}{\text{Particle Diameter}} = \frac{D}{d}$
5.85	1.28	2.54	1.98
6.82	0.90	2.03	2.26
6.34	1.04	2.29	2.20
5.21	1.96	3.81	1.94
5.04	1.56	3.05	1.96
3.91	2.84	4.70	1.65
9.99	0.52	1.35	2.60
9.96	0.45	1.31	2.89
11.76	0.48	1.40	2.92
10.58	0.52	1.40	2.69
10.56	0.52	1.44	2.77
10.40	0.46	1.31	2.85
12.12	0.39	0.97	2.49
12.48	0.39	1.06	2.72
13.83	0.33	0.93	2.82
13.13	0.45	1.30	2.88
13.38	0.30	0.85	2.83
9.73	0.52	1.35	2.60
10.73	0.58	1.35	2.33
10.83	0.56	1.52	2.71
9.47	0,61	1.57	2.57
9.53	0.60	1.59	2.65
9.45	0.63	1.71	2.70
14.19	0.34	1.02	3.04
13.56	0.42	1.27	3.02
15.27	0.28	0.89	3.18
15.54	0.37	1.14	3.08
9.51	0.56	1.48	2.64
8.35	0.76	1.84	2.42
7.40	0.94	2.03	2.16
7.70	0.94	2.29	2.44
7.62	0.91	2.10	2.31

TABLE II - Cratering Results from Iron Particles Impacting a 0.0002" Stainless Steel Foil. No particles completely penetrated the foil.

Particle Velocity (km/sec)	Particle Diameter (microns)	Crater Diameter (microns)	$\frac{\text{Crater Diameter}}{\text{Particle Diameter}} = \frac{D}{d}$
2.84	2.48	2.79	1.13
2.72	2.06	2.67	1.30
2.81	1.81	2.41	1.33
3.16	2.60	2.92	1.12
3.50	3.62	4.23	1.17
3.73	2.30	3.56	1.55
5.48	1.76	3.68	2.09
4.68	2.24	4.11	1.83
4.53	2.12	3.81	1.80
4.56	2.02	2.79	1.38
5.14	1.84	3.45	1.88
5.30	1.48	3.18	2.15
4.99	1.96	3.81	1.94
5.99	1.46	3.12	2.14
6.72	0.93	2.11	2.27
7.15	1.04	2.49	2.39
6.71	1.16	2.74	2.36
7.17	0.85	1.98	2.33

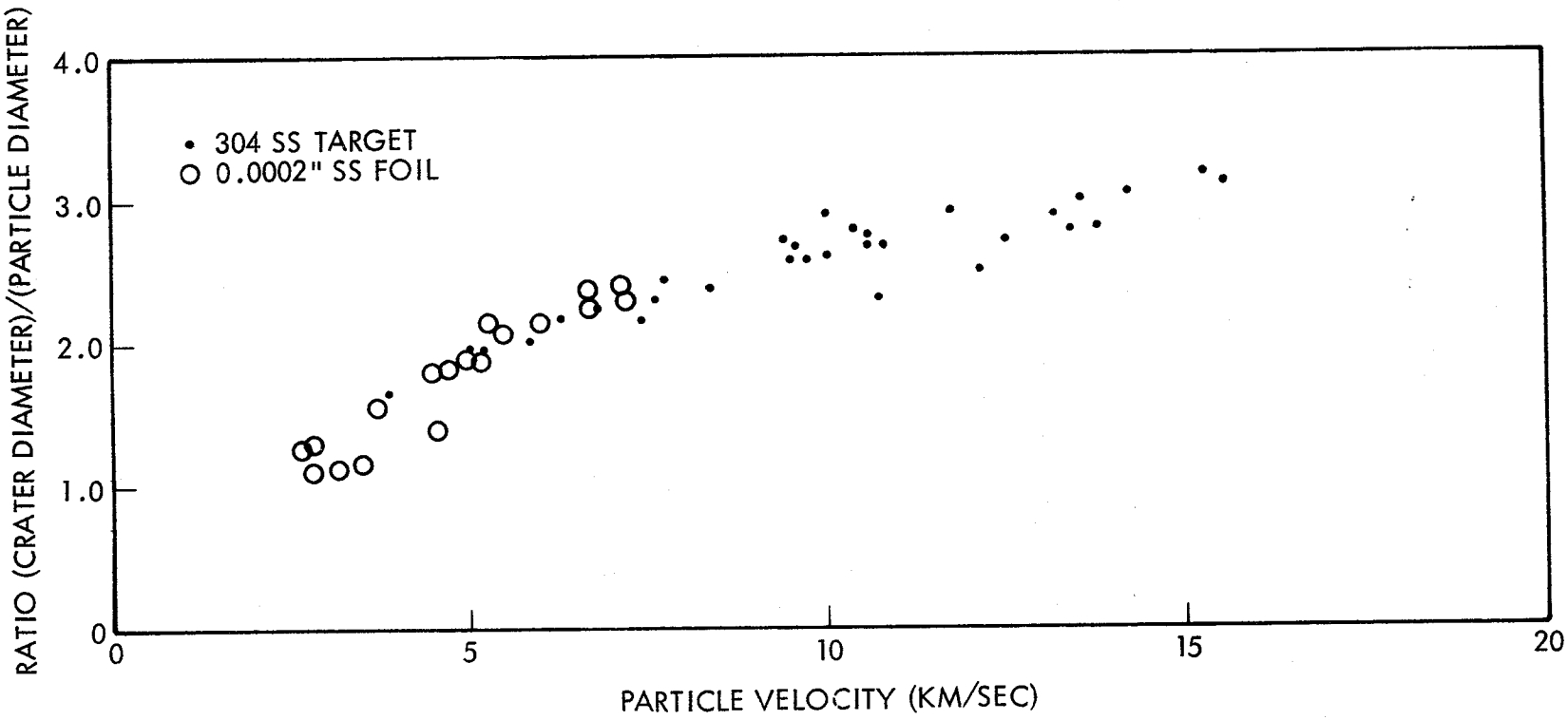

Figure 15. Ratio of crater diameter to impacting particle diameter as a function of particle velocity for iron particles impacting stainless steel.

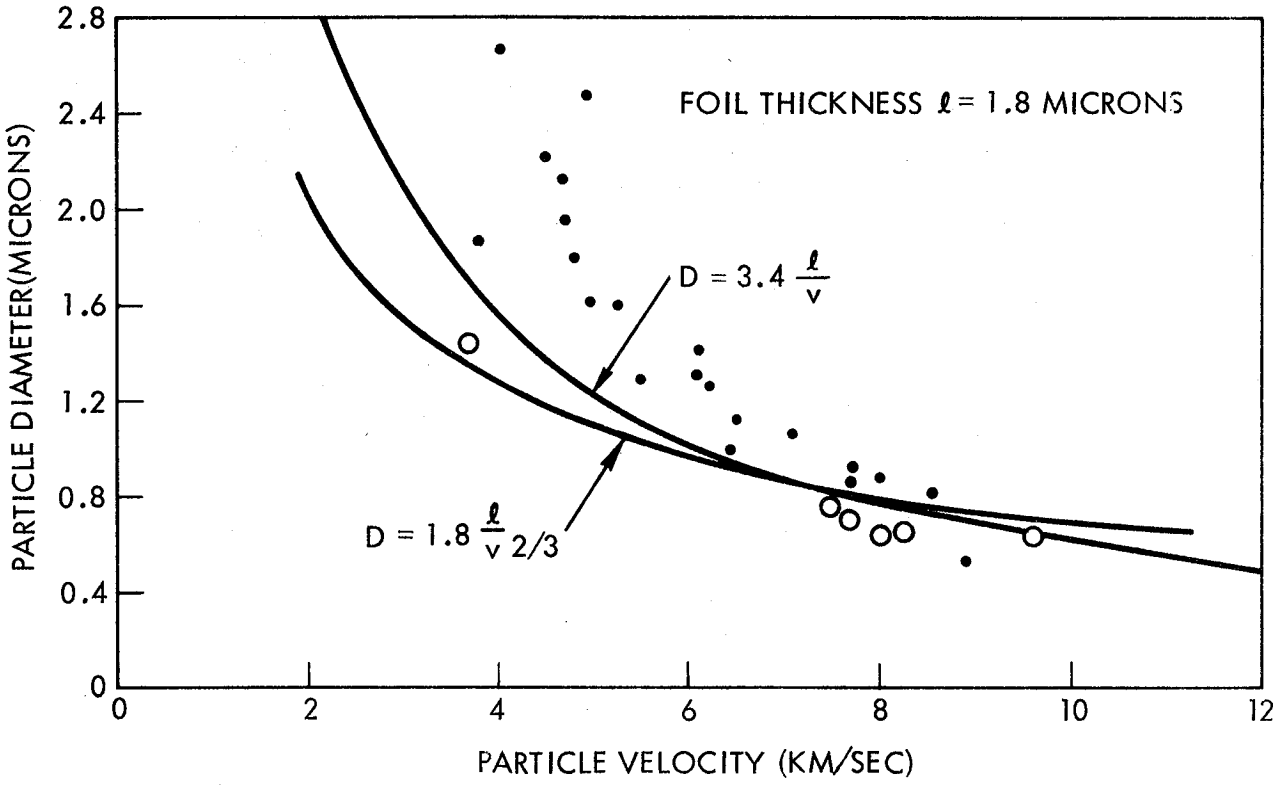

Figure 16. Particle diameter versus particle velocity to show penetration of thin foils. Foil was 1.8 micron thick nickel. Solid points are particles which penetrate the foil, open points are particles which did not penetrate. See text for explanation of curve shown in figure.

and the open circles are those which did not penetrate. With the exception of one maverick point at 8.9 km/sec, in the region between 7 and 9 km/sec one can clearly define a line above which particles penetrate and below which they fail to do so.

It has been suggested that perhaps a variation in foil thickness could account for the "maverick point" mentioned above. This is a distinct possibility since it is undoubtedly more difficult to control uniformity in thickness with these very thin foils. However, an attempt was made to avoid any region of the foil which had pinholes and might be subject to this problem.

In an attempt to quantify the relationship between particle diameter and probability of penetration, we have arbitrarily assumed that the diameter required for penetration varies inversely as the velocity to the 2/3 power. With this assumption, a curve is drawn which is normalized to a diameter of 0.8 microns at 8 km/sec. Because of the clustering of points between 7 and 9 km/sec it is possible to define the curve very accurately there.

The resultant curve, using the usual linear relationship to foil thickness is shown in Figure 16. It states that penetration will occur when the particle radius d exceeds a minimum size given by

$$d > 1.8\ \ell/v^{2/3} \qquad (7\text{-}1)$$

where ℓ, the foil thickness, and d have the same dimensional units and the particle velocity v is in (km/sec).

The fact that one point (at 8.9 km/sec) falls below the curve in what is otherwise a very clean experiment is annoying. Of course there is always the possibility of an error in data recording or calculation. We have rechecked the data on that particular point and can find nothing wrong. Since there appears to be no good reason for discarding it, it is left in.

It was suggested by NASA-Langley that perhaps a better fit could be obtained with the penetration data if a diameter dependence on V^{-1} was assumed. In following this suggestion, another curve has been drawn and is defined by

$$d = 3.4 \frac{\ell}{v} \qquad (7\text{-}2)$$

where ℓ is again the foil thickness, v the impact velocity, and ℓ and d have the same dimensional units. This curve was normalized to a diameter of 0.8 micron at 7.7 km/sec. Again the curve should be well defined at this location due to the tight clustering of points. This curve is at least an equally good fit to the data and perhaps better than equation (7-1), although unfortunately the data points are not positioned so as to clearly define which function is the more correct one.

A further check of the penetration curves is provided by the data on the 1.27 micron foil. These points are plotted in Figure 17 as particle diameter versus velocity with solid points representing penetrations. Both curves predict that all the particles should penetrate the foil and this is precisely what happened. This kind of evidence may hardly be considered conclusive, but it is certainly not in disagreement with Equation (7-1) and (7-2).

We have one more piece of evidence and that is the data obtained on the 0.0002" stainless steel foil. If we treat the steel foil as equivalent to nickel foil (the densities are similar, Ni = 8.9, SS = 7.75), we may see whether equations (6-1) and (6-2) predict the results obtained on the SS foil. These data are shown in Figure 18 again as particle diameter versus particle velocity and all are plotted as open circles since all failed to penetrate the foil. Also shown in Figure 18 is equations (7-1) and (7-2). Both curves lie comfortably above the points, as expected. Again this is not very conclusive evidence, but it shows a consistent agreement.

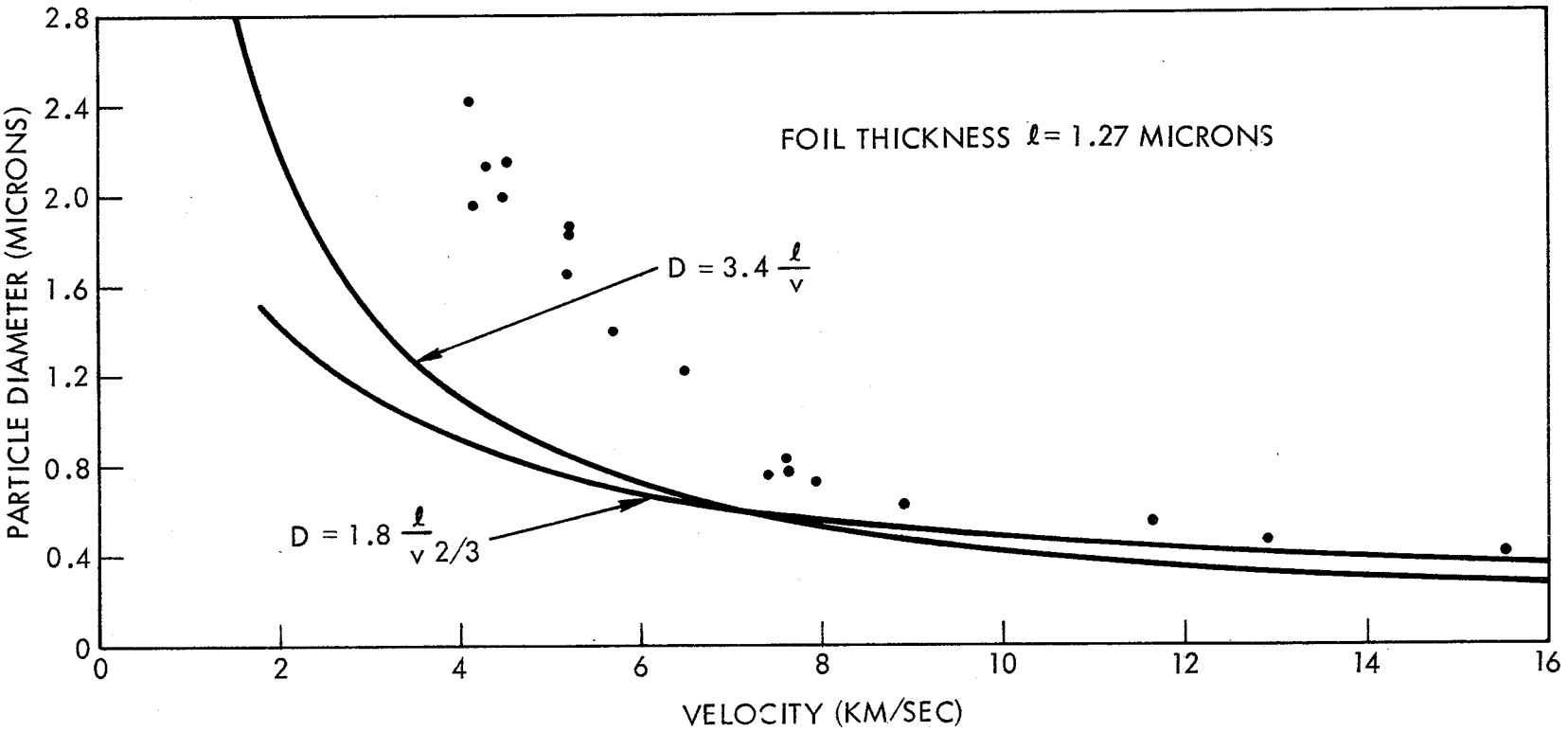

Figure 17. Particle diameter versus particle velocity to show penetration of thin foils. Foil was 1.27 micron thick nickel. Solid points are particles which penetrate the foil, open points are particles which did not penetrate. See text for explanation of curve shown in figure.

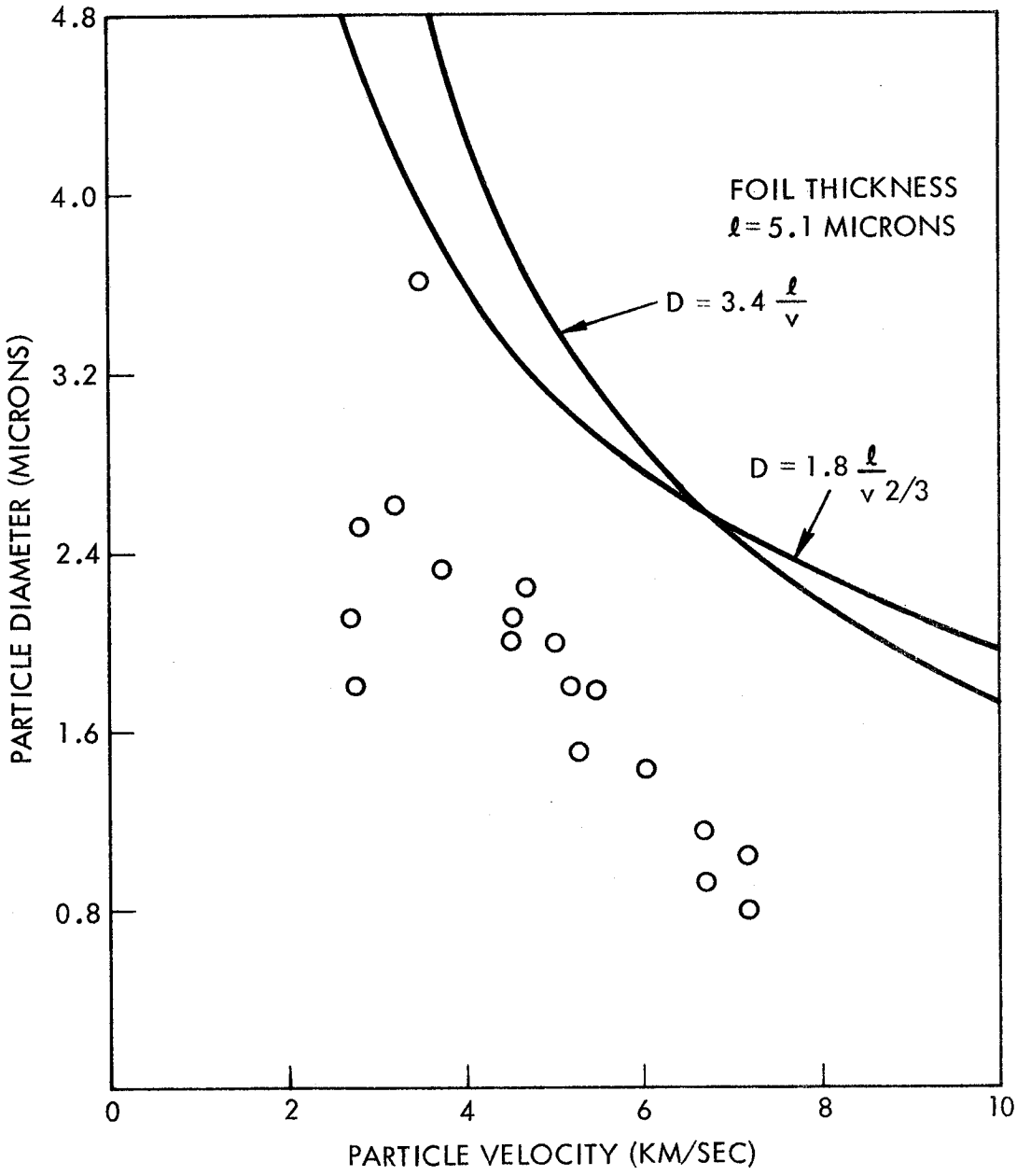

Figure 18. Particle diameter versus particle velocity to show penetration of thin foils. Foil was 0.0002" thick stainless steel. Solid points are particles which penetrate the foil, open points are particles which did not penetrate. See text for explanation of curve shown in figure.

7.3 PHOTOGRAPHS OF PENETRATIONS

It is relatively easy to determine whether or not a given particle has penetrated the foil. As discussed above, all the impact points were located with an optical microscope and then by backlighting the target a complete penetration was immediately apparent.

However, all the impact points were examined in the scanning electron microscope, providing further confirmation. Furthermore, we went to some trouble to photograph both the entrance and exit side of the penetrations. This is a somewhat laborious procedure and only enough time was available to do the 1.8 micron foil. Some of these pictures are shown in Figures 19 through 23. Each figure shows the entrance side on the left and the exit side of the same hole on the right.

One of the most interesting pair of photographs is shown in Figure 23. On the left is a photograph of the entrance side of a particle which failed to penetrate completely. On the back side of the foil we were able to locate the same point and this photograph is shown on the right side of the figure. It appears as a bump on the back side of the foil. It is highly interesting that there is no evidence of spalling even though the material has been considerably distended.

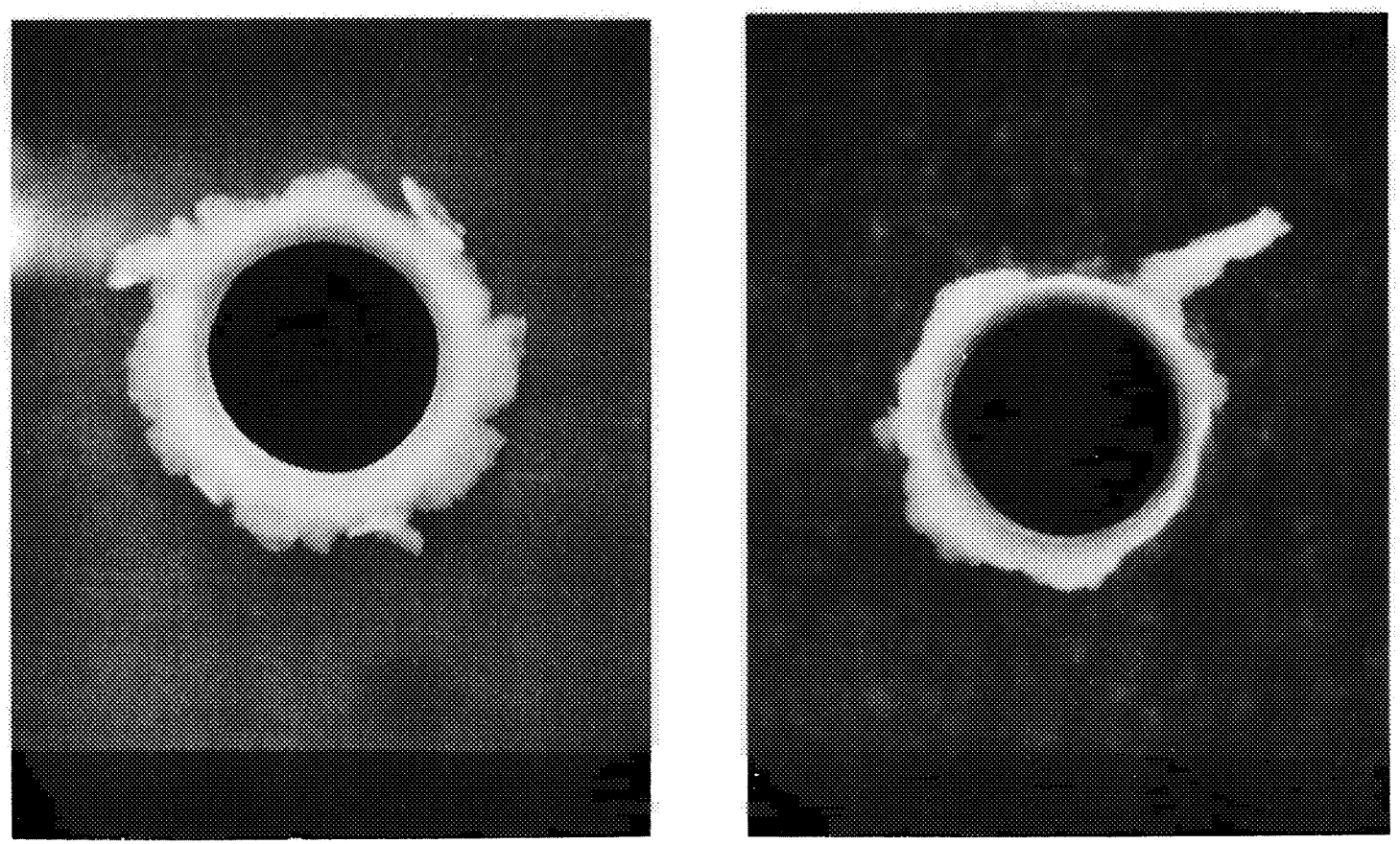

Exit Side

Target Material - 1.8 Micron Nickel Foil
Projectile - Iron
Diameter - 1.6 Microns
Mass - 1.7×10^{-14} Kgm
Impact Velocity - 5.25 km/sec
Crater Diameter - 3.2 Microns
Magnification - 10,000

Figure 19. Photographs from scanning electron microscope of penetration in a 1.8 micron nickel foil. Left hand photograph shows entrance side and right hand photograph exit side of same penetration. Magnification, hole diameter and particle parameters given above.

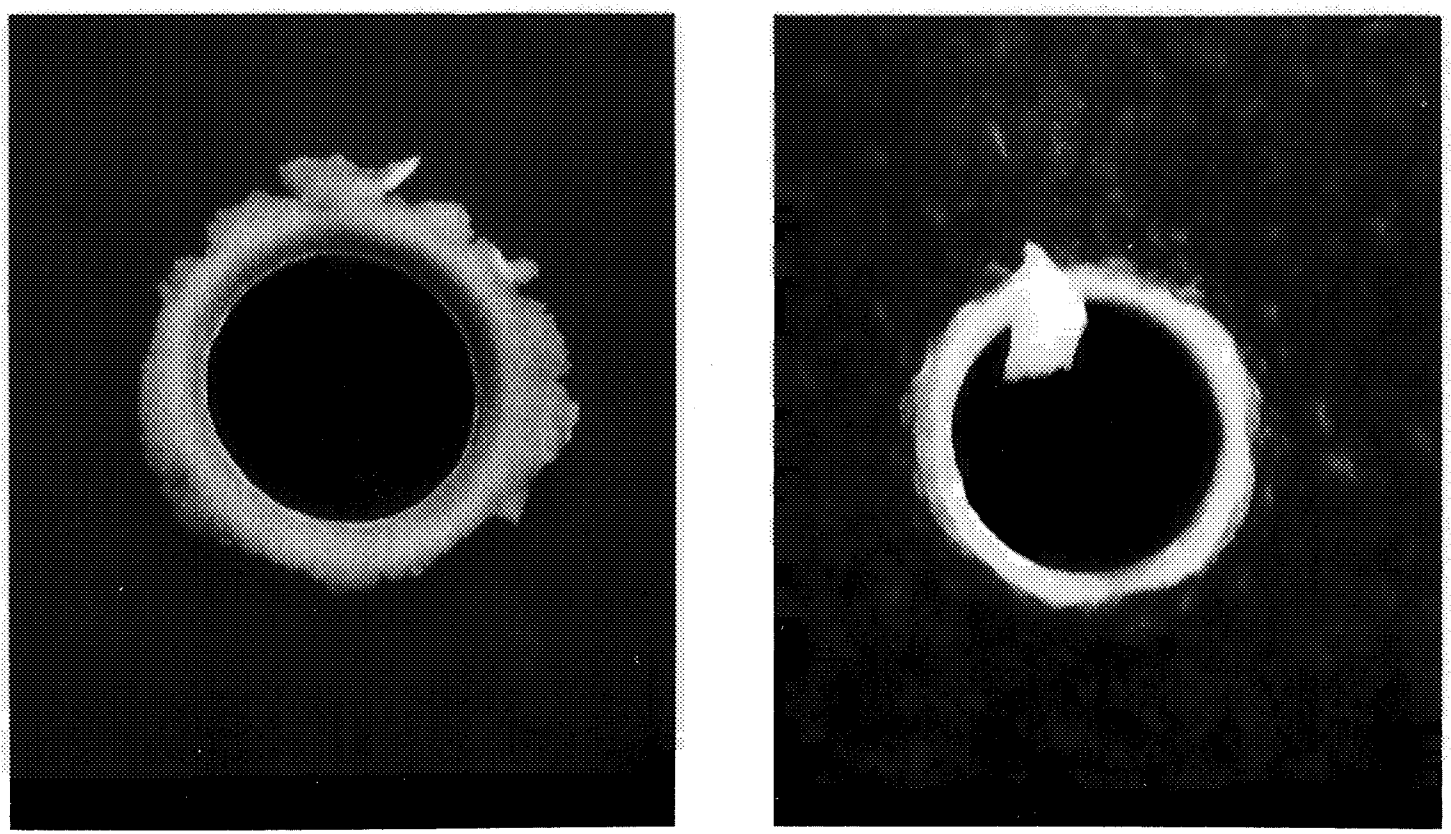

Exit Side

Target Material - 1.8 Micron Nickel Foil
Projectile - Iron
Diameter - 2.7 Microns
Mass - 7.6 x 10^{-14} Kgm
Impact Velocity - 3.98 km/sec
Crater Diameter - 3.6 Microns
Magnification - 10,000

Figure 20. Photographs from scanning electron microscope of penetration in a 1.8 micron nickel foil. Left hand photograph shows entrance side and right hand photograph exit side of same penetration. Magnification, hole diameter and particle parameters given above.

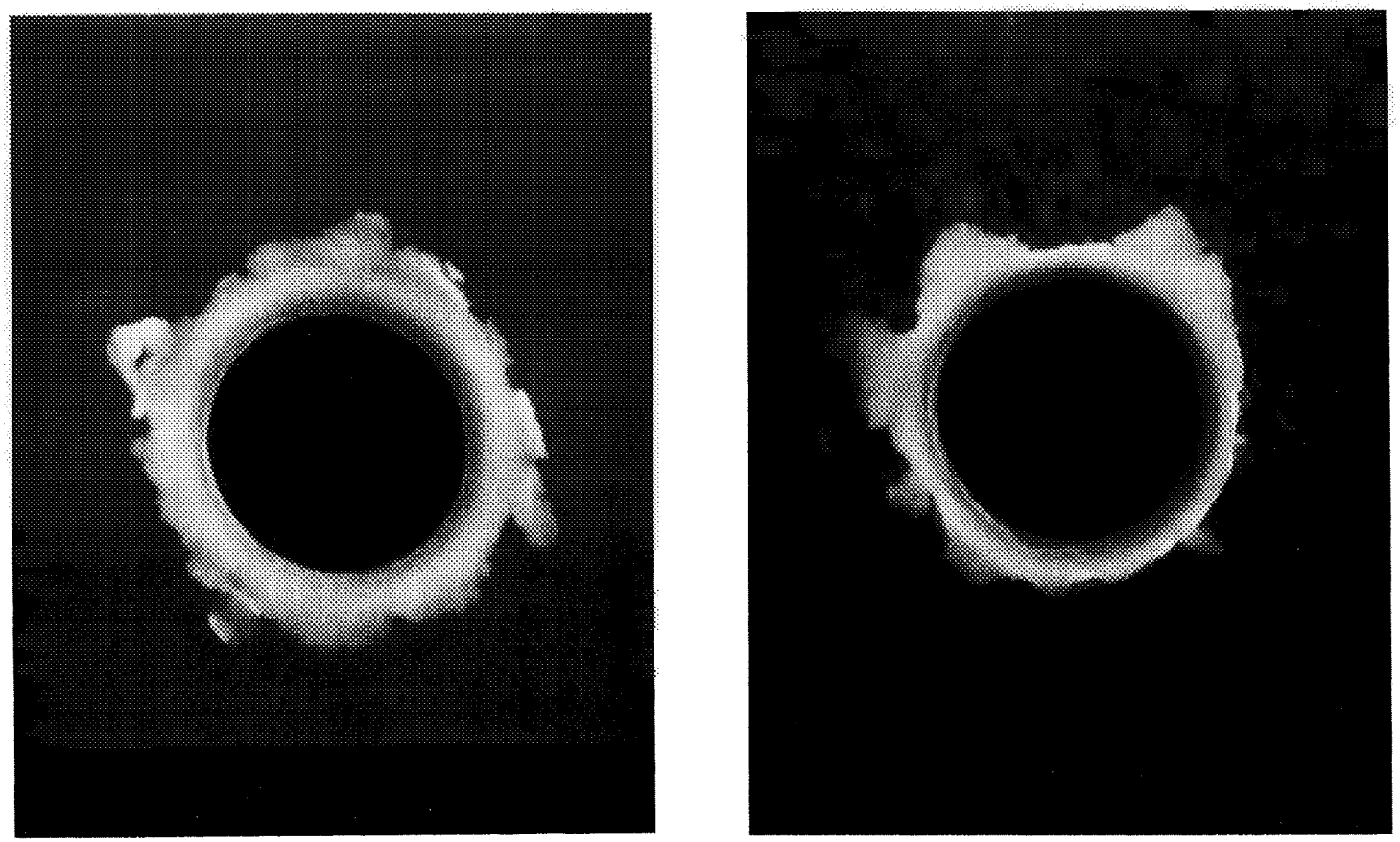

Exit Side

Target Material - 1.8 Micron Nickel Foil
Projectile - Iron
Diameter - 2.0 Microns
Mass - 3.0×10^{-14} Kgm
Impact Velocity - 4.67 km/sec
Crater Diameter - 3.6 Microns
Magnification - 10,000

Figure 21. Photographs from scanning electron microscope of penetration in a 1.8 micron nickel foil. Left hand photograph shows entrance side and right hand photograph exit side of same penetration. Magnification, hole diameter and particle parameters given above.

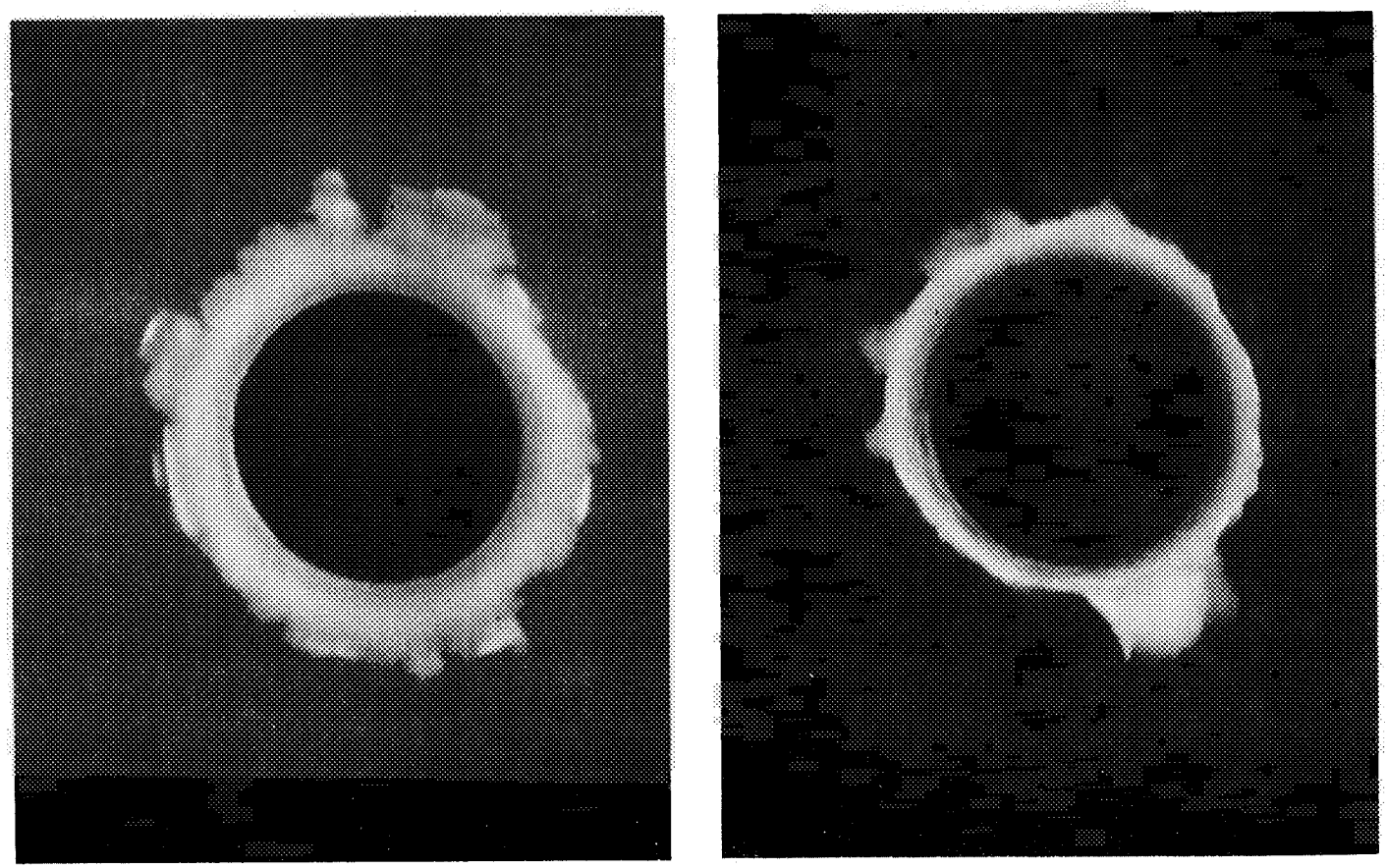

Exit Side

Target Material - 1.8 Micron Nickel Foil
Projectile - Iron
Diameter - 2.1 Microns
Mass - 3.9 x 10^{-14} Kgm
Impact Velocity - 4.72 km/sec
Crater Diameter - 3.9 Microns
Magnification - 10,000

Figure 22. Photographs from scanning electron microscope of penetration in a 1.8 micron nickel foil. Left hand photograph shows entrance side and right hand photograph exit side of same penetration. Magnification, hole diameter and particle parameters given above.

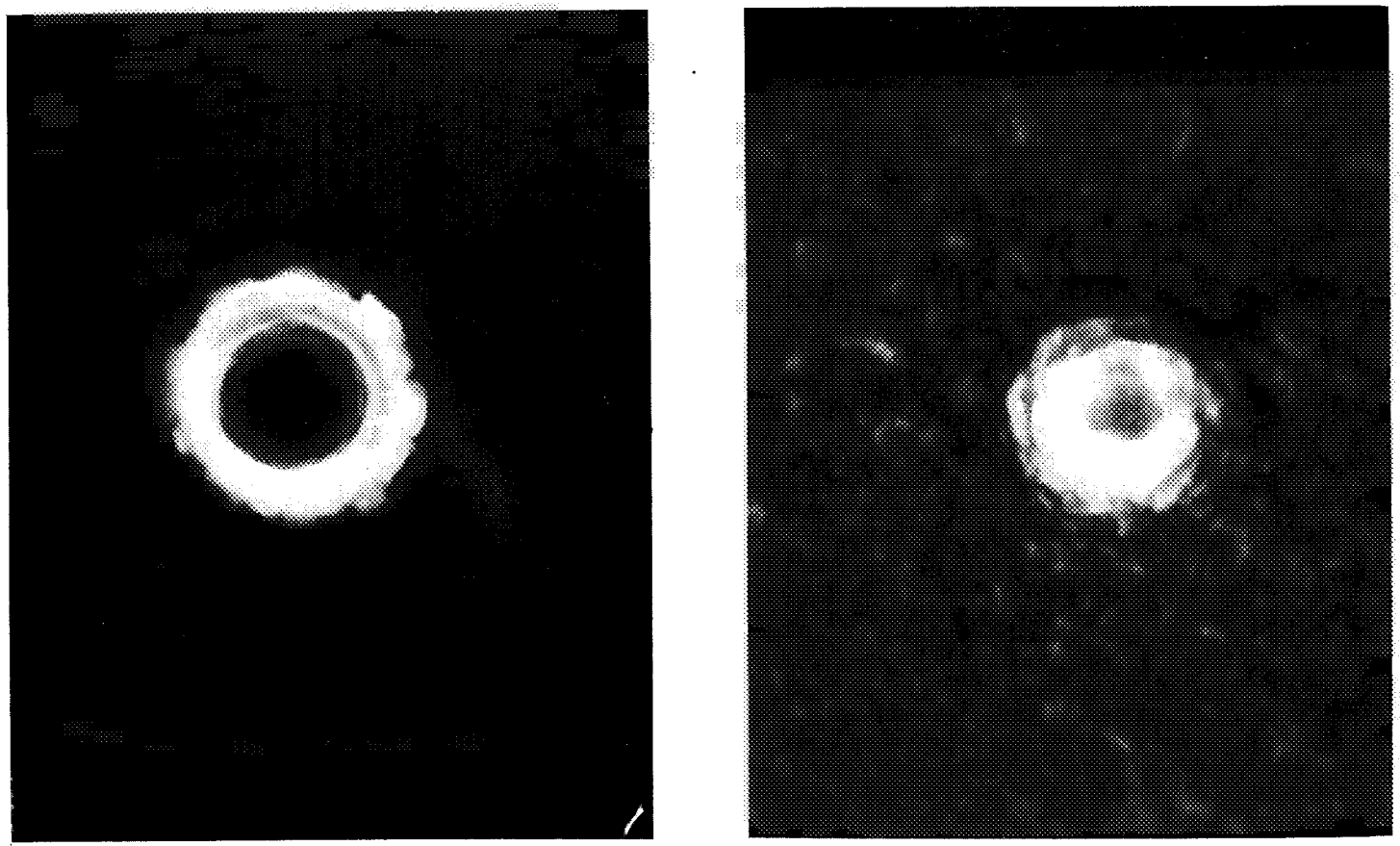

Exit Side

Target Material - 1.8 Micron Nickel Foil
Projectile - Iron
Diameter - 2.1 Microns
Mass - 3.9×10^{-14} Kgm
Impact Velocity - 4.72 km/sec
Crater Diameter - 3.9 Microns
Magnification - 10,000

Figure 23. Photographs from scanning electron microscope of penetrations in a 1.8 micron nickel foil. Left hand photograph shows entrance side and right hand photograph exit side of same penetration. Magnification, hole diameter and particle parameters given abo

REFERENCES

1. Friichtenicht, J. F.: Two-Million-Volt Electrostatic Accelerator for Hypervelocity Research. Rev. of Sci. Inst., Vol. 33, pp. 209-212, February, 1962.

2. Slattery, J. C.; and Becker, D. G.: Theoretical and Experimental Studies Relating to the Use of a Linear Accelerator for Micrometeoroids. Final report, April 1967, NASA CR-66466.

3. Friichtenicht, J. F.; and Slattery, J. C.: Ionization Associated with Hypervelocity Impact. NASA TN D-2091, 1963.

4. Friichtenicht, J. F.; Slattery, J. C.; and Tagliaferri, E.: A Laboratory Measurement of Meteor Luminous Efficiency. The Astrophysical Journal, Vol. 151, pp. 747-758, February, 1968.

5. Hansen, D. O.: Mass Analysis of Ions Produced by Hypervelocity Impact. Applied Physics Letters, Vol. 13, No. 3, pp. 89-91, August, 1968.

6. Hansen, D. O.; and Roy, N. L.: A Solid-State Low-Noise Preamplifier. Nuclear Instruments and Methods, Vol. 40, pp. 209-212, 1966.

7. Denardo, B. Pat; Summers, James L.; and Nysmith, C. Robert: Projectile Size Effects on Hypervelocity Impact Craters in Aluminum. NASA TN D-4067, 1967.

8. Slattery, J. C.; and Friichtenicht, J. F.: Experimental Research on Hypervelocity Cratering by Microscopic Particles. TRW Systems Report 03246-6001-R000 (Contract NASw-1116, Final Report), November, 1966.